Title

Single-Cell RNA-seq Reveals Profound Alterations in Mechanosensitive Dorsal Root Ganglion Neurons with Vitamin E Deficiency.

Authors

Finno, Carrie J
Peterson, Janel
Kang, Mincheol
et al.

Publication Date

2019-11-01

DOI

10.1016/j.isci.2019.10.064

Peer reviewed

iScience

CellPress

Article

Single-Cell RNA-seq Reveals Profound Alterations in Mechanosensitive Dorsal Root Ganglion Neurons with Vitamin E Deficiency

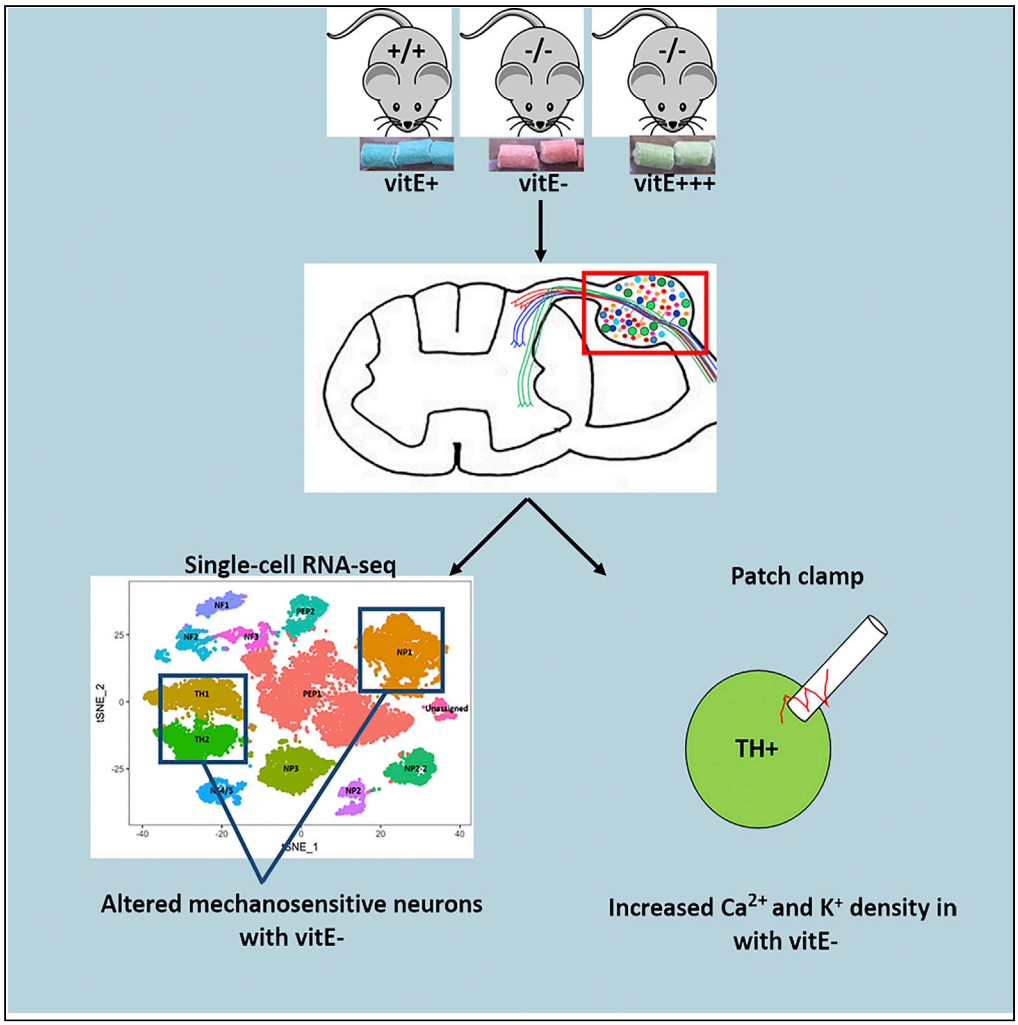

Carrie J. Finno, Janel Peterson, Mincheol Kang, ..., Maria C. Perez-Flores, Jeong H. Lee, Ebenezer N. Yamoah

cjfinno@ucdavis.edu

HIGHLIGHTS

vitE deficiency alters gene expression in DRGs

Mechanosensitive TH+ DRG neurons are most affected

K^+ and Ca^{2+} current densities are increased in vitE-deficient TH+ DRG neurons

High-dose vitE supplementation prevents the molecular phenotype

Finno et al., iScience 21, 720–735
November 22, 2019
https://doi.org/10.1016/j.isci.2019.10.064

iScience

CellPress

Article

Single-Cell RNA-seq Reveals Profound Alterations in Mechanosensitive Dorsal Root Ganglion Neurons with Vitamin E Deficiency

Carrie J. Finno,[1,4,*] Janel Peterson,[1] Mincheol Kang,[2] Seojin Park,[2] Matthew H. Bordbari,[1] Blythe Durbin-Johnson,[3] Matthew Settles,[3] Maria C. Perez-Flores,[2] Jeong H. Lee,[2] and Ebenezer N. Yamoah[2]

SUMMARY

Ninety percent of Americans consume less than the estimated average requirements of dietary vitamin E (vitE). Severe vitE deficiency due to genetic mutations in the tocopherol transfer protein (*TTPA*) in humans results in ataxia with vitE deficiency (AVED), with proprioceptive deficits and somatosensory degeneration arising from dorsal root ganglia neurons (DRGNs). Single-cell RNA-sequencing of DRGNs was performed in *Ttpa*$^{-/-}$ mice, an established model of AVED. In stark contrast to expected changes in proprioceptive neurons, *Ttpa*$^{-/-}$ DRGNs showed marked upregulation of voltage-gated Ca^{2+} and K^{+} channels in mechanosensitive, tyrosine-hydroxylase positive (TH+) DRGNs. The ensuing significant conductance changes resulted in reduced excitability in mechanosensitive *Ttpa*$^{-/-}$ DRGNs. A highly supplemented vitE diet (600 mg dl-α-tocopheryl acetate/kg diet) prevented the cellular and molecular alterations and improved mechanosensation. VitE deficiency profoundly alters the molecular signature and functional properties of mechanosensitive TH+ DRGN, representing an intriguing shift of the prevailing paradigm from proprioception to mechanical sensation.

INTRODUCTION

A mere 10% of the adult American population consume the estimated average requirements (EARs) of vitamin E (vitE) (~15 mg/day α-tocopherol [α-TOH]) (Fulgoni et al., 2011; Institute of Medicine, 2000; Maras et al., 2004). Severe vitE deficiency stemming from liver diseases, extensive intestinal resections, and the inherited disease of vitE deficiency termed "ataxia with vitE deficiency" (AVED) result in profound ataxia (Muller, 2010). Prevailing functions of vitE have been ascribed to the maintenance of typical neurologic structure and function. Despite identification of vitE as an essential food nutrient (Brigelius-Flohe and Traber, 1999), the molecular, cellular, and functional mechanisms of vitE remain debated. There is extensive evidence supporting the role of vitE, specifically α-tocopherol (α-TOH), as a lipid-soluble antioxidant *in vitro* (Niki, 2014) and *in vivo* (Choi et al., 2015; McDougall et al., 2017), and this has been suggested to be the primary functional mechanism of biologic activity (Traber and Atkinson, 2007). Besides this well-established role as an inhibitor of lipid peroxidation, other non-antioxidant properties of α-TOH have been identified, including transcriptional regulation and cell signaling (Azzi, 2018).

AVED results from mutations in the α-tocopherol transfer protein gene (*TTPA*) (Gotoda et al., 1995; Yokota et al., 1996). Phenotypic variability is due the location of the genetic mutation within *TTPA*, the amount of vitE in the daily diet, and the time of initiation and dosage of vitE supplementation (Bellayou et al., 2009; Di Donato et al., 2010). Most patients demonstrate symptoms of AVED between 4 and 18 years of age (Cavalier et al., 1998; Gotoda et al., 1995; Schuelke, 1993). Patients with AVED exhibit ataxia, areflexia, decreased fine touch, and vibration discrimination (Gotoda et al., 1995; Schuelke, 1993). Histologic hallmarks of AVED include axonal swellings within the dorsal column medial lemniscus pathway, the sensory pathway that conveys sensations of fine touch vibration, two-point discrimination, and proprioception from the skin and joints. Of note, lesions in the gracile system of the medulla oblongata are also features of physiologic neuroaxonal aging across many species (Bridge et al., 2009). Chronic vitE, specifically α-TOH, deficiency slowly accelerates brain lipid peroxidation and results in cognitive impairment in mice (Fukui et al., 2015) and zebrafish (McDougall et al., 2017). These deficits can be partially restored by vitE supplementation, in the form of α-TOH. Indeed, early α-TOH supplementation in patients with AVED may suppress severe disease symptoms by unknown mechanisms (Aparicio et al., 2001).

[1]Department of Population Health and Reproduction, School of Veterinary Medicine, University of California, Davis, CA 95616, USA

[2]Department of Physiology, School of Medicine, University of Nevada, Reno, Reno, NV 89557, USA

[3]Bioinformatics Core Facility, Genome Center, University of California, Davis, CA 95616, USA

[4]Lead Contact

*Correspondence: cjfinno@ucdavis.edu

https://doi.org/10.1016/j.isci.2019.10.064

Ttpa$^{-/-}$ mice represent an accepted model that recapitulates the phenotype of AVED, with ataxia and histologic lesions, including reduction of myelinated fibers in the gracile fasciculus and chromatolysis of neurons within the nucleus gracilis, as early as 6 months of age (Finno et al., 2018). By 17 months of age, diminished dendritic branching of Purkinje neurons within the cerebellum is evident (Ulatowski et al., 2014). The affected somatosensory tracts originate in the dorsal root ganglia (DRG), with apoptosis of DRG neurons (DRGNs) evident by 12 months of age (Finno et al., 2018). Therefore, it has been suggested that the most pronounced neurologic deficit in *Ttpa*$^{-/-}$ mice is loss of proprioception. This proprioceptive loss and associated pathology in the spinal cord and cerebellum can be prevented by supplementation of *Ttpa*$^{-/-}$ mice at weaning with 17x the amount of dl-α-tocopheryl acetate (600 mg/kg feed) (Finno et al., 2018). These studies demonstrate that the interaction of genotype, dietary vitE concentration, and time point in postnatal development are crucial to the development of the neurologic phenotype.

To investigate the underlying mechanisms of functional alterations with vitE deficiency, single-cell RNA-sequencing (scRNA-seq) was performed within the DRG of *Ttpa*$^{-/-}$ mice. We hypothesized that the most profound transcriptional dysregulation with vitE deficiency would occur in large-diameter myelinated proprioceptive DRGNs. Therefore, we sought to (1) define the transcriptional dysregulation within DRGN subpopulations in *Ttpa*$^{-/-}$ mice and (2) identify alterations in membrane electrical properties within the targeted DRGN subpopulations of *Ttpa*$^{-/-}$ mice.

RESULTS

Single-Cell RNA-Sequencing Defines Specific DRGN Subpopulations

To determine the molecular mechanisms leading to sensory deficits in vitE-deficient DRGNs, scRNA-seq was performed on neuronal cells collected from the DRG (between cervical [C1] and lumbar [L6] vertebrae) of mice in three experimental groups: (1) *Ttpa*$^{+/+}$ on a basal vitE diet (vitE+; WT), (2) *Ttpa*$^{-/-}$ on vitE-deficient diet (DEF), and (3) *Ttpa*$^{-/-}$ on vitE-supplemented diet (SUPP) at 6 months of age (Table S1; see Methods for dietary vitE levels). We have previously identified clinicohistologic evidence of the ataxic phenotype by 6 months of age and completed whole tissue transcriptomic profiling of spinal cord and cerebellum at this time point (Finno et al., 2018). In that study, we identified only minor differences between *Ttpa*$^{-/-}$ mice maintained on a basal diet (i.e. 35 mg of dl-α-tocopheryl acetate/kg feed) and *Ttpa*$^{-/-}$ mice on a vitE-deficient diet (DEF; <10 mg of dl-α-tocopheryl acetate/kg feed). Instead, a highly supplemented vitE diet (SUPP; 600 mg of dl-α-tocopheryl acetate/kg feed) was required to prevent the AVED phenotype. Therefore, in the current study, we focused our comparisons on DEF vs. WT and DEF vs. SUPP mice. Contrasts included (1) WT vs. DEF, to determine gene expression changes associated with severe vitE deficiency in DRGNs; (2) SUPP vs. DEF to determine the biologic mechanisms whereby the clinicopathologic AVED phenotype is prevented; and (3) SUPP vs. WT to identify any remaining dysregulated pathways following high-dose vitE supplementation in *Ttpa*$^{-/-}$ mice. As high-dose vitE supplementation does not restore brain α-TOH to WT concentrations (Finno et al., 2018; Yokota et al., 2001), we postulated that any gene dysregulation within the SUPP vs. WT group may provide insight into this phenomenon.

ScRNA-seq was performed on an average of 3,614 ± 470 DRGN from two replicate mice per group, with a total of 382 million (M) reads generated (17,862 ± 2,625 reads/cell). Approximately 66.5% of reads mapped to the murine transcriptome, similar to previous reports (Usoskin et al., 2015), and an average of 1,788 ± 283 genes detected per cell, with no difference between experimental groups (Figure S1).

Unsupervised single-cell transcriptome profiling identified 14 initial subpopulations in all mice, using gene profiles as previously reported (Figures 1A and S2A) (Usoskin et al., 2015; Li et al., 2016). Based on further evaluation of subpopulations 0 and 2, both clusters appeared to contain peptidergic neurons and were, therefore, merged into cluster 0.2 (Figure S2B). The top transcripts in each subpopulation are provided in Table S2. A t-distributed stochastic neighbor embedding (t-SNE) plot identified a small number of neuronal cells that could not be classified based on previously reported gene profiles (Figure S2A). This cluster was labeled as "Unassigned." Each DRG subpopulation set contained differentially expressed genes characteristic for that cluster. These clusters were classified as PEP1, PEP2, NP1, NP2, NP2-2, NP3, NF1, NF2, NF3, NF4-5, TH1, and TH2 as previously described (Usoskin et al., 2015) and "Unassigned" for the unassigned cluster (Table S2). There were no significant differences in cell count per neuronal cluster across experimental groups ($p > 0.05$ in each subpopulation) (Table S1). A distinct population of microglial cells based on previously reported markers was not identified (Figure 1A). Although previous studies have identified outliers or cells with unresolved identity, we further evaluated the "Unassigned" DRGN

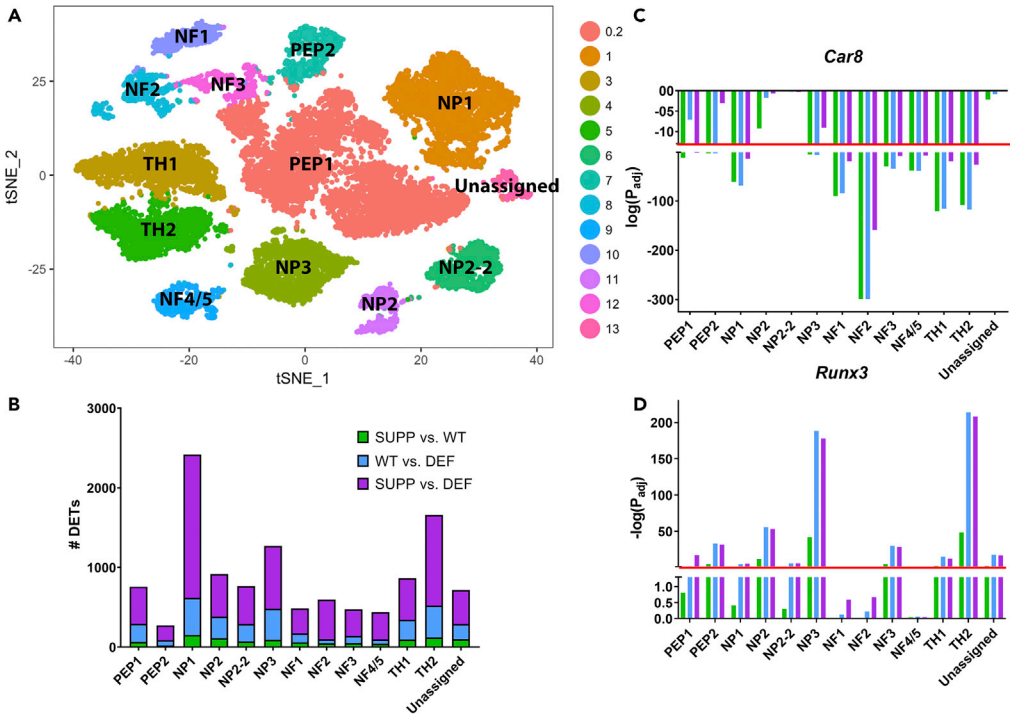

Figure 1. An Overall Increase in the Number of Differentially Expressed Transcripts across All DRGN Subpopulations with α-TOH Deficiency

(A) A t-distributed stochastic neighbor embedding (t-SNE) plot of merged datasets of the six experimental mice to define neuronal subpopulations clusters. Thirteen clusters were identified based on previously reported gene expression profiles (Li et al., 2016; Usoskin et al., 2015). The "NP2-2" subgroup contained some genes representative of the NP2 cluster but was distinct from the NP2 cluster and has been previously characterized (Usoskin et al., 2015; Li et al., 2016). (B) An increasing number of significantly (P_{FDR}<0.05) differentially expressed transcripts (DETs) was identified in each DRGN subpopulation with increasing contrasts of vitE deficiency (i.e. SUPP vs. DEF > WT vs. DEF > SUPP vs. WT). (C and D) (C) The two most commonly dysregulated transcripts across DRGN subpopulations were carbonic anhydrase 8 (*Car8*), which was significantly downregulated in 10/13 DRG clusters with vitE deficiency (SUPP vs. DEF), and (D) the lineage-specific transcription factor *Runx3*, which was significantly upregulated in 10/13 DRG clusters with vitE deficiency (SUPP vs. DEF). p values were adjusted by a false discovery rate of 0.05 and log-transformed. Significance was set at P_{FDR}<0.05, corresponding to a –log $P_{adjusted}$>1.3 (red line). NF = neurofilament, NP = non-peptidergic, PEP = peptidergic, TH = tyrosine hydroxylase, UNKNOWN = unknown cluster, n = 2 mice per group with ~3,600 cells/mouse profiled.

subpopulation using the top 15 transcripts defining this cluster (Figure S2A, Table S2). Two of the most specific transcripts representing this cluster, forkhead box protein transcription factor 2 (*Foxp2*) and olfactomedin 3 (*Olfm3*), have been previously identified in DRG, primarily in postnatal mice through P14 (Jia et al., 2018; Nakaya et al., 2012). However, these transcripts are also present in adult brain (Ferland et al., 2003; Nakaya et al., 2012; Saunders et al., 2018). Therefore, this subset of neurons most likely represents the small number of remaining developmental neurons undergoing axonal growth.

An Increasing Number of Dysregulated Transcripts with Increasing vitE Deficiency

Within each neuronal cluster, dysregulated transcripts were identified between WT vs. DEF, SUPP vs. WT, and SUPP vs. DEF. For each cell subpopulation, at least two-fold dysregulated (i.e. up- or downregulated at P_{FDR}<0.05) transcripts were identified between vitE treatment groups (i.e. SUPP vs. DEF >> WT vs. DEF > SUPP vs WT) (Figure 1B, Tables S3 and S4). The greatest degree of dysregulation in the SUPP vs. DEF group was apparent in the NP1 and TH2 subpopulations (Figure 1B).

Top Dysregulated Transcripts across the Majority of DRG Subpopulations: *Car8* and *Runx3*

When WT and SUPP were compared with the DEF groups, carbonic anhydrase 8 (*Car8*), encoding for a protein that inhibits inositol trisphosphate receptor 1 (IP_3R1) (Zhuang et al., 2015), was significantly (P_{FDR}<0.05) downregulated in 10/13 DRG clusters (Figure 1C). In particular, *Car8* was the top downregulated transcript

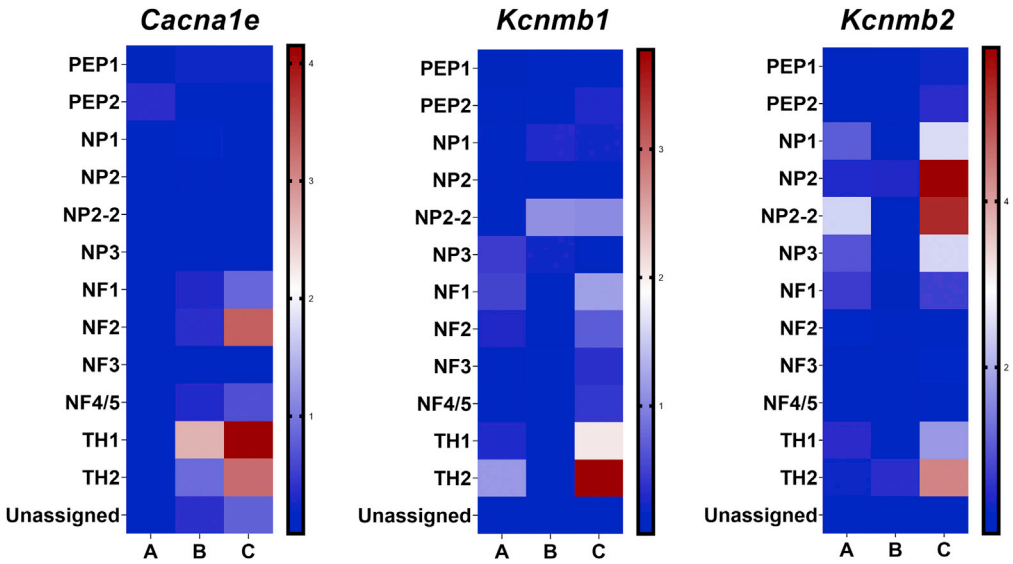

Figure 2. Upregulation Intermediate Voltage-Gated Ca^{2+} and K^+ Channels in TH+ DRGNs with vitE Deficiency

Heatmaps, plotted by $-\log P_{adjusted}$, comparing the degree of upregulation for R-type intermediate voltage-gated Ca^{2+}, *Cacna1e*, and Ca^{2+}-activated K^+ channel beta subunits channels, *Kcnmb1* and *Kcnmb2*, in DRGN subpopulations with vitE deficiency. Contrast A = SUPP vs. WT, contrast B = WT vs. DEF, contrast C = SUPP vs DEF. *Cacna1e*= Cav2.3 intermediate voltage-activated Ca^{2+} channel, *Kcnmb* = Potassium large conductance calcium-activated channel, subfamily M, beta.

with vitE deficiency in the four neurofilament subgroups (NF1, NF2, NF3, and NF4/5). *Car8* was downregulated in these subgroups even in the SUPP vs. WT contrast (Figure 1C). The lineage-specific transcription factor *Runx3* was significantly (P_{FDR}<0.05) upregulated in 10/13 DRG clusters when comparing WT and SUPP vs. DEF groups, especially within NP3 and TH2 (Figure 1D). Even within the SUPP vs. WT contrast, *Runx3* remained significantly upregulated in 8/13 DRG subpopulations, including NP3 and TH2 (Figure 1D).

As Car8 is the primary inhibitor of IP_3R1 (Hirasawa et al., 2007; Hirota et al., 2003) and transcription of *Car8* was significantly downregulated with vitE deficiency, we postulated that IP_3R1 signaling might be affected by the level α-TOH supplementation. In DEF mice, a pronounced decrease in IP_3R1 was apparent in TH+ DRGNs, whereas protein levels appeared increased in SUPP mice (Figure S3A). Similarly, Car8 was increased in TH+ DRGNs in the SUPP group (Figure S3B).

Profound Upregulation of Voltage-Gated Ca^{2+} and K^+ Channels in TH+ DRGNs

Modulation of Ca^{2+} channel activities mediate changes in neuronal plasticity and, when upregulated, promote neurodegeneration (Chilton, 2006). Transcripts associated with both ligand-gated and voltage-gated Ca^{2+} and K^+ channels were evaluated across genotype and vitE diet groups in our scRNA-seq dataset (Table S5). When comparing SUPP vs. DEF groups, of the voltage-activated Ca^{2+} channels expressed in DRGNs, intermediate-voltage $Ca_v2.3$ (*Cacna1e;* TH1 $P_{FDR} = 1.51 \times 10^{-8}$, TH2 $P_{FDR} = 1.29 \times 10^{-11}$) channel was most notably upregulated in TH+ DRGNs (Figure 2A). High-voltage-activated P-type Ca^{2+} channel, *Cacna1a,* was not significantly altered in any DRGN subpopulation, whereas N-type Ca^{2+} channel, *Cacna1b,* was only upregulated in the NP1 DRGN subpopulation of the SUPP vs. DEF groups ($P_{FDR} = 0.001$) (Table S5). When evaluating K^+ channel transcripts significantly (P_{FDR}< 0.05) upregulated in the SUPP vs. DEF groups, the most commonly affected DRGN subpopulations for K^+ voltage-gated channel transcript upregulation were TH+ (Table S5). In particular, regulatory subunits of the large-conductance Ca^{2+}-activated channel subfamily M (*Kcnmb1;* TH1 $P_{FDR} = 0.009$, TH2 $P_{FDR} = 1.68 \times 10^{-4}$ and *Kcnmb2;* TH1 $P_{FDR} = 0.017$, TH2 $P_{FDR} = 5.20 \times 10^{-5}$) were upregulated in TH+ DRGNs (Figure 2B). Although a few of the transcripts encoding voltage-gated K^+ channels were upregulated in TH+ DRGNs, most transcripts in this family were upregulated in the non-peptidergic DRGNs (Table S5).

Increase in Cacna1e and Kcnmb2 with vitE Deficiency in TH+ DRG

To confirm that $Ca_v2.3$ (*Cacna1e*) and regulatory subunits *Kcnmb1* and *Kcnmb2* were indeed upregulated, we further evaluated mRNA and protein levels of Cacna1e and Kcnmb2. In DEF mice, there was a

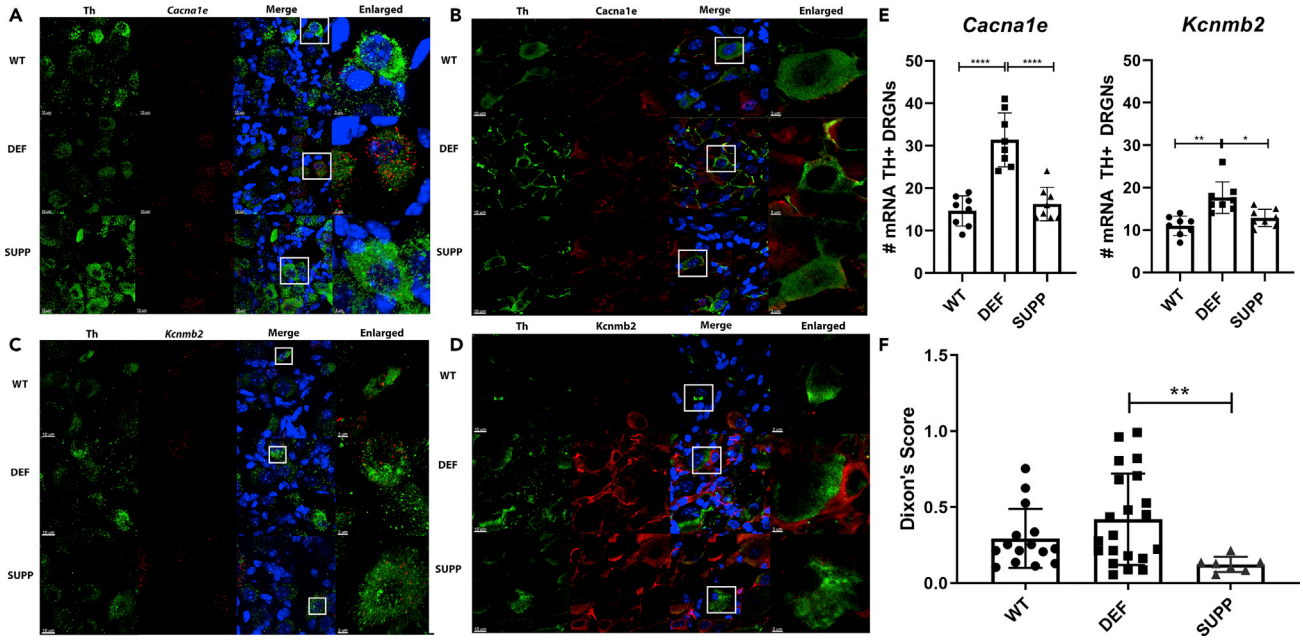

Figure 3. Increase in Cacna1e and Kcnmb2 with vitE Deficiency in TH+ DRG

(A–D) Green: Th, Blue: DAPI nuclei, Red: Cacna1e [(A) mRNA, (B) protein] and Kcnmb2 [(C) mRNA, (D) protein]. White box inset magnified in the last column. Fluorescent immunohistochemistry from 4-month WT, DEF, and SUPP mice, n = 1–2 per group. Scale bars represent 10 μm (TH, Cacna1e, Kcnbm2, and merge) and 3 μm (enlarged).

(E) Quantification of mRNA using RNAscope for *Cacna1e* and *Kcnmb2*. Mean ± SD, N = 8 counts per experimental group, one-way ANOVA, or Kruskal-Wallis. Scale bars represent 10 μm (TH, Cacna1e, Kcnbm2, and merge) and 3 μm (enlarged).

(F) Von Frey assay, demonstrating a significant increase in sensitivity (i.e. lower Dixon's score) in the SUPP vs. DEF mice. Mean ± SD, N = 8–22 per group, one-way ANOVA, ****p< 0.0001, **p< 0.01, *p< 0.05.

pronounced increase in *Cacna1e* and *Kcnmb2* in TH+ DRGNs at the level of both mRNA (Figures 3A, 3C, and 3E) and respective proteins (Figures 3B and 3D).

Supplementation with High-Dose α-TOH Increased Mechanical Sensitivity in *Ttpa*$^{-/-}$ Mice

The von Frey filament assay was performed as previously described (Martinov et al., 2013). SUPP mice had significantly increased mechanical sensitivity compared with DEF diet ($P_{adjusted}$ = 0.007, Figure 3F).

Altered Excitability of *DEF* Small-Diameter DRGNs

To understand the etiology and mechanisms of DRG neuronal responses, sensory deficits, and degeneration in AVED as shown in *Ttpa*$^{-/-}$ mice (Finno et al., 2018; Yokota et al., 2001), we focused on the changes in membrane electrical properties. First, we focused on identifying small-diameter mechanosensitive DRGNs. We applied displacement-clamp at DRGN cell-bodies. Using a holding potential of −70 mV, mechanical displacement of the small-diameter DRGN cell body evoked inward currents (Figure 4A, inset shows traces from WT DRGN). The mechanically activated (MA) current (I_{MA}) had amplitudes ranging from 75 to 500 pA (*n* = 11; Figure 4A). The displacement-response relationships from data from WT DRGNs were fitted with a single Boltzmann function with half-maximal activation displacement ($X_{1/2}$) and slope factor of 1.1 ± 0.1 μm and 0.3 ± 0.1 μm (*n* = 11; Figure 4A). Similar data from *DEF* DRGNs for $X_{1/2}$ and slope factor were 1.5 ± 0.1 μm and 0.4 ± 0.1 μm (n = 7). Unpaired ttest comparison shows significant differences in the $X_{1/2}$ (p = 0.016) but not the slope factor (p = 0.51) between the WT and DEF DRGNs. The rightward shift in the displacement-response relations in the DEF DRGNs suggest a decrease in mechanical sensitivity.

Three functional classes of neurons were then assessed based on their evoked spike frequency adaptation kinetics, defined as fast (eliciting 1–2 APs for ~0.5-s suprathreshold current injection), medium (4–6 APs), and slow (>10 APs) adapting neurons. We first compared WT with DEF DRGNs. On average, the input resistances of the three classes of neurons in WT were ~2-fold greater than the DEF neurons. Figures 4B and

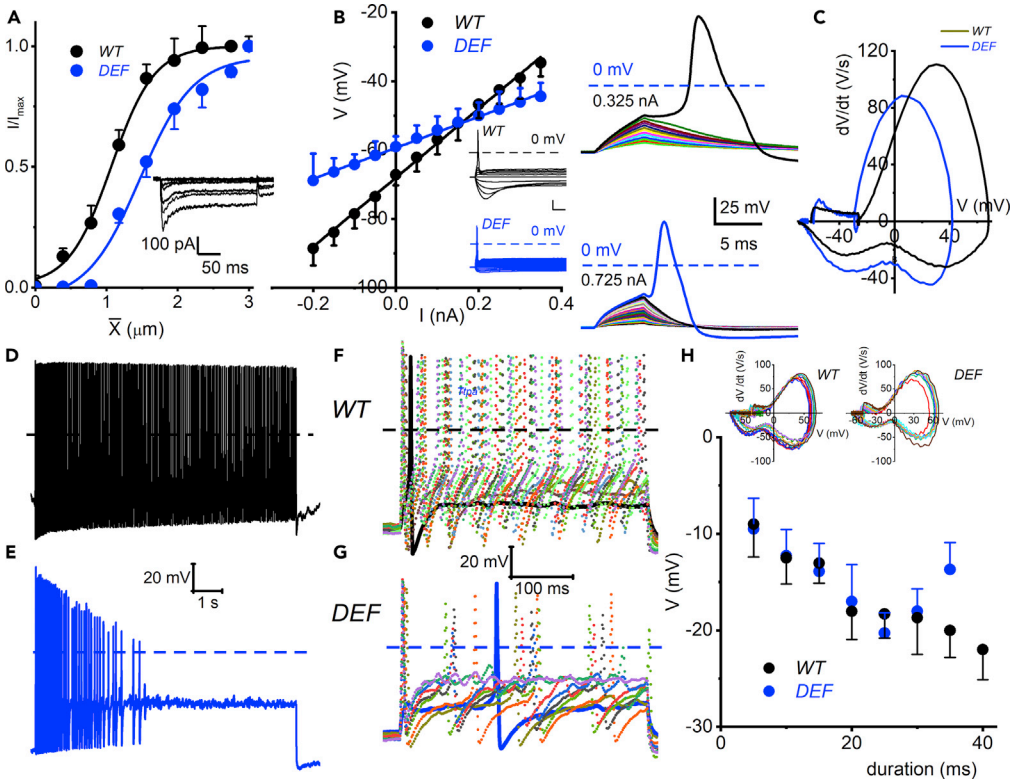

Figure 4. Membrane Properties of Small-Diameter Dorsal Root Ganglion Neurons (DRGNs) from WT and DEF Mice

Current-clamp recordings were performed on DRGNs 6-month-old mice. Membrane input resistance (R_i) was determined by evaluating membrane voltage changes in response to negative and positive current injection. The ohmic relations were fitted with linear regression and the R_i derived from the slope.

(A) Representative traces of displacement-clamp currents recorded using CsCl/NMG-based pipette solution in response to ~250-ms mechanical displacement steps of ~0.42 μm to WT small-diameter DRGN (shown as inset). DRGNs were held at −70 mV. Summary data of displacement-response relationship of mechanically activated (MA) currents (I_{MA}) represented as the I/I_{max} or open channel probability (P_o) against displacement (X) fitted with single Boltzmann function. Data from WT DRGNs (shown in black symbols and fitted with sigmoidal curve in black) and the one-half maximum displacements ($X_{1/2}$) are 1.1 ± 0.1 μm and 0.3 ± 0.1 μm (n = 11). Data from DEF DRGNs (shown in blue symbols and fitted with sigmoidal curve in blue) and the one-half maximum displacements ($X_{1/2}$) are 1.5 ± 0.1 μm and 0.4 ± 0.1 μm (n = 7).

(B) Among the small-diameter neurons, there were three distinct classes: fast, medium, and slow adapting. Exemplary plots from fast-adapting DRGNs from WT mice (shown in black, mean R_i in MΩ; 100 ± 6; n = 15), and in DEF (shown in blue, mean R_i in MΩ; 45 ± 5; n = 17: p< 0.0001). The inset is an example of data used to generate the plots. For medium-adapting neurons the R_i (in MW) were as follows: WT (306 ± 23; n = 9) and DEF (162 ± 29; n = 11: p = 0.0014). For slow-adapting neurons the R_i were WT (626 ± 47; n = 13) and DEF (395 ± 38; n = 11: p = 0.0012).

(C) Brief (~5 ms) stepwise positive current was injected to elicit subthreshold (shown in different color codes) and threshold depolarization (WT in black and DEF in blue). The threshold currents are indicated. The threshold voltage was determined, using a dV/dt loop plot (inset, right).

(D and E) Typical voltage response from slow-adapting DRGNs recorded from WT and DEF mice.

(F and G) Action potentials generated using varying pulse durations from fast-adapting DRGNs in WT (F) and DEF (G) mice.

(H) Plots of the relations between threshold potential and pulse duration in WT (in black) and DEF (in blue) mice. The insets show the dV/dt *versus* membrane potential (V) loops used to determine the thresholds.

4C summarize exemplary steady-state input resistances (R_i, in MΩ), of the WT (black; 100 ± 6; n = 15), with ~0.33 nA required to elicit an AP and DEF (blue; 45 ± 5; n =17), with ~0.73 nA being the AP threshold for fast-adapting DRGNs. For medium-adapting neurons, the R_i were WT (306 ± 23; n = 9) and DEF (162 ± 29, = 11), and for slow-adapting neurons the R_i were WT (626 ± 47; n = 13) and DEF (395 ± 38; n = 11). The intrinsic membrane properties of the small-diameter DRGNs suggested that membrane excitability was reduced in DEF mice. In agreement with this assertion, DEF slow-adapting DRGNs showed profound

attenuation in spike activity in response to current injection compared with WT DRGNs (Figures 4D and4E). AP thresholds for fast-adapting DRGNs were determined by calculating dV/dt, as illustrated in Figure 4C (right panel), and the sensitivity of neurons were tested using the indicated pulse duration. For WT DRGNs, with increasing pulse duration, the threshold voltage amplitude declined in a monotonic fashion. However, for DEF DRGNs, the threshold voltage had a biphasic response relative to pulse duration (Figures 4F–4H).

Increased K^+ and Ca^{2+} Density in *DEF* Small-Diameter DRGNs

The underlying conductances responsible for the reduced R_i and membrane excitability in the small-diameter *Ttpa*$^{-/-}$ DRGNs were examined in the voltage-clamp configuration. Ca^{2+} and K^+ currents were isolated under conditions where other ion channel conductances were suppressed. The rationale for focusing on these Ca^{2+} and K^+ conductances stemmed from the scRNAseq analyses (Figures 2 and 3). Whole-cell voltage-clamp of the small-diameter mechanosensitive DRGNs showed outward K^+ currents with transient and sustained components in both WT (Figure 5A, upper panel, black) and DEF (Figure 5A, lower panel, blue) mice in response to varying voltage steps (−110 to 40 mV) from a holding potential of −90 mV in 10-mV increments. The difference-current traces plotted in dashed lines (inset) provide the profile of the enhanced outward K^+ current in the DEF DRGNs. This difference in currents consisted of mainly a sustained outward current. The total outward K^+ current density plotted as a function of voltage showed significant differences in current densities elicited at −30 to 40 mV step voltages comparing data between WT and DEF mice ($n = 17$; $p < 0.05$, Figure 5B). To examine Ca^{2+} currents, we suppressed outward K^+ currents, by substituting pipette and bath K^+ with $NMDG^+$ and Cs^+ (see Methods). Inward Na^+ current contamination of Ca^{2+} currents was suppressed using TTX (1 μM) and by partial substitution of bath Na^+ with NMDG. Ca^{2+} currents were activated using −90 and −40 mV holding voltages, and varying step voltages were applied from −120 to 40 mV. Ca^{2+} currents in DRGN consist of multiple components: low- and high-voltage-activated currents (Boland and Dingledine, 1990; Wu and Pan, 2004). The difference-current derived by subtracting current traces generated from −40 mV and that at −90 mV holding potentials yielded mainly the transient and low-voltage activated components (Figures 5C and 5D). Summary data from current-voltage relations show that the high-voltage-activated Ca^{2+} currents were enhanced in DEF DRGNs (Figure 5E). As shown in the inset and illustrated in the current-voltage, rSNX-482 (500 nM), a $Ca_v2.3$ (R-type) current-specific blocker (Xie et al., 2016), suppressed a component of the Ca^{2+} current. Additionally, in three recordings from DEF DRGNs, in which rSNX-482 was applied in the bath solution, the enhanced current was attenuated, suggesting the current was conducted by $Ca_v2.3$ channels (Catterall et al., 2005; Xie et al., 2016).

Since high-dose vitE supplementation on DEF DRGN appeared to restore the molecular and cellular hallmarks of vitE deficiency, we examined the membrane properties of small-diameter DRGNs in SUPP mice. We examined sensitivity of SUPP DRGNs to mechanical displacements as described in Figure 4A. The displacement-response relationships from data from SUPP DRGNs were fitted with a single Boltzmann function (shown in green) with half-maximal activation displacement ($X_{1/2}$) and slope factor of 1.09 ± 0.1 μm and 0.3 ± 0.1 μm ($n = 6$; Figure 6A). We superimposed data from WT (in black) and DEF (in blue) DRGNs for comparison. A one-way ANOVA was performed to compare the $X_{1/2}$ and the slope factor in WT, DEF, and SUPP DRGNs displacement-response curves. There were significant differences at the $p < 0.05$ level for the three conditions ($X_{1/2}$ $F(2,21) = 6.088$, $p = 0.008$). Post-hoc comparisons using the Tukey HSD test indicated that data from WT and DEF ($p = 0.011$) as well as DEF and SUPP ($p = 0.024$) are significantly different. There was no significant difference between WT and SUPP. Additionally, there were no significant differences in the slope factor in the three experimental conditions.

Excitability of *SUPP* Small-Diameter DRGNs

For SUPP mice, fast-adapting DRGNs had a mean R_i 115 ± 9 MΩ ($n = 11$) (Figure 6B, shown with green symbols and line). The R_i between WT (in black line), DEF (in blue line), and DRGNs (Figure 4B) is replotted for comparison. There were significant differences at the $p < 0.05$ level for the three conditions ($F(2,40) = 174.7$, $p = 0.001$). Post-hoc comparisons using the Tukey HSD test indicated that R_i from WT vs. DEF ($p = 0.001$), WT vs. SUPP ($p = 0.001$), and DEF vs. SUPP ($p = 0.001$) are significantly different. Similar to WT DRGNs, as the pulse duration was prolonged, the threshold voltage amplitude declined (Figure 6C). However, the apparent preventative effects of vitE supplementation were not visibly seen in the slow-adapting small-diameter DRGNs. Compared with WT DRGNs, the slow-adapting neurons in SUPP did not recover fully despite vitE supplementation (Figure 6D). We examined whole-cell onward K^+ currents by applying depolarizing voltage steps from −130 to 30 mV (ΔV = 10 mV), from a holding potential of −90 mV in SUPP DRGNs (Figure 6E). The steady-state outward K^+ currents normalized to individual membrane capacitance (C_m)

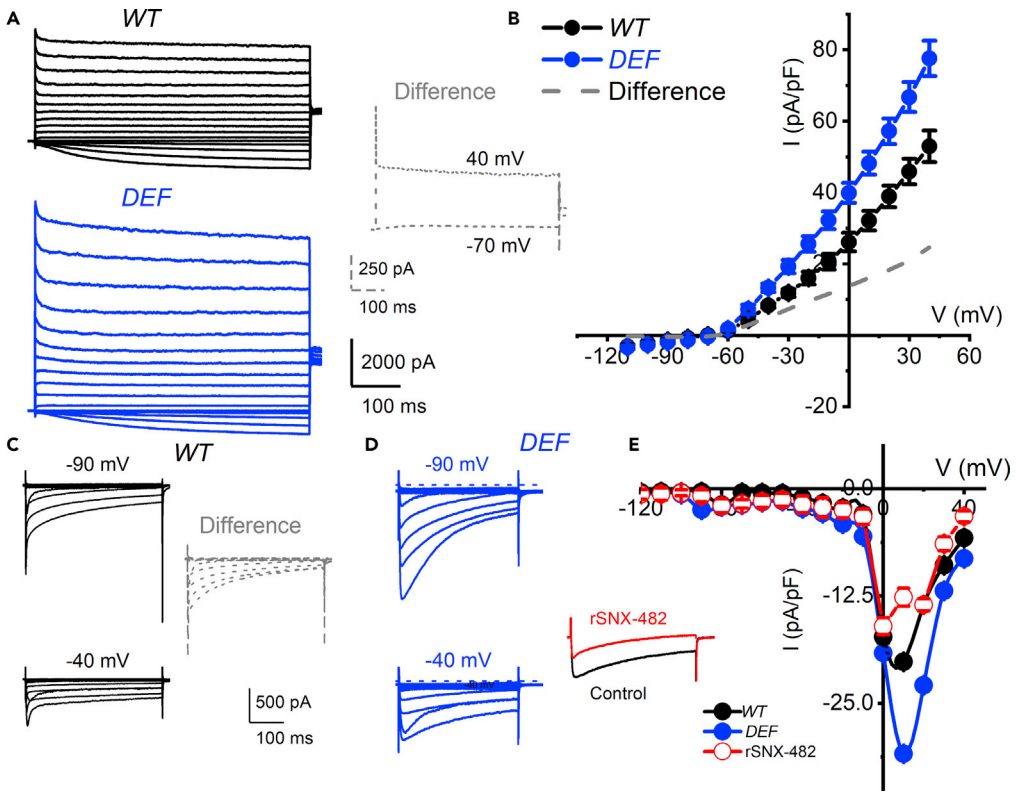

Figure 5. Increased K^+ and Ca^{2+} Current Density in DEF versus WT DRGNs

(A)Whole-cell onward K^+ currents were elicited using depolarizing steps from −110 to 40 mV (ΔV = 10 mV). The tail currents were at −40 mV. Current traces recorded from WT and DEF DRGNs are shown in black and blue, respectively. To obtain a profile of currents that are enhanced in DEF DRGNs, we determined the "difference currents" between DEF and WT neurons at −70 and 40 mV step voltages (traces are plotted with dashed lines in inset).

(B) Summary of steady-state currents was normalized to individual membrane capacitance (C_m), from 6-month-old WT mice (shown with black line and symbol) and *DEF* (shown with gray traces). Data were generated from 14 DRGNs from each experimental group. The mean current densities (in pA/pF) in WT and DEF DRGNs at 0 mV step voltage were 26.1 ± 2.6 and 39.9 ± 2.8; n = 14, p = 0.0015.

(C and D) Inward Ca^{2+} currents recorded from a 12-pF DRGNs in WT (in black) and DEF (in blue) mice from −90 and −40 mV holding potentials. Currents were generated using voltage steps ranging from −110 to 40 mV. The difference-current traces (−90 mV) - (−40 mV) are plotted in dashed lines as an inset.

(E) Peak Ca^+ current density (I)-voltage (V) relation from data amassed from 12 DRGNs in each group. The current densities generated from a holding voltage of −40 mV are plotted with WT in black and DEF in blue. The high-voltage activated component of the Ca^{2+} current was enhanced in the DEF DRGNs. The peak current density (in pA/pF) for currents elicited from a holding potential of −40 mV for WT DRGNs was 20.1 ± 1.5 (n = 9) and for DEF DRGNs was 30.9 ± 2.5 (n = 9, p = 0.002). After application of 500 nM rSNX-482 to the DEF DRGNs the peak current density plummeted to 12.6 ± 1.2 (n = 6, p< 0.0001).

(Figure 6F) showed that vitE supplementation is sufficient to restore the outward K^+ current (plotted in green and compared with the mean data from WT [in black] and DEF [in blue]) (see Figure 5B). For example, the total outward current density elicited at 0 mV in SUPP DRGNs was 24.7 ± 2.9 pA/pF (n = 11). There were significant differences at the p< 0.05 level for the three conditions; steady-state K^+ current elicited at 0 mV F(2,36)= 47.6, p = 0.001. Post-hoc comparisons using the Tukey HSD test indicated that WT vs. DEF (p = 0.001) and DEF vs. SUPP (p = 0.001) are significantly different. There is no significant difference between WT vs. SUPP (p = 0.58). We recorded inward Ca^{2+} currents from ~10-pF DRGNs in SUPP mice using −90 and −40 mV holding voltages. Currents were generated using voltage steps ranging from −120 to 40 mV (Figures 6G and 6H). The current-voltage relations generated at −90 mV and −40 mV holding voltages are plotted, and the data suggest that vitE supplementation seemingly reversed the enhanced high-voltage-activated Ca^{2+} current observed in DEF DRGNs (Figure 6I). Summary data from DEF DRGNs in Figure 5E (in blue) is replotted for comparison.

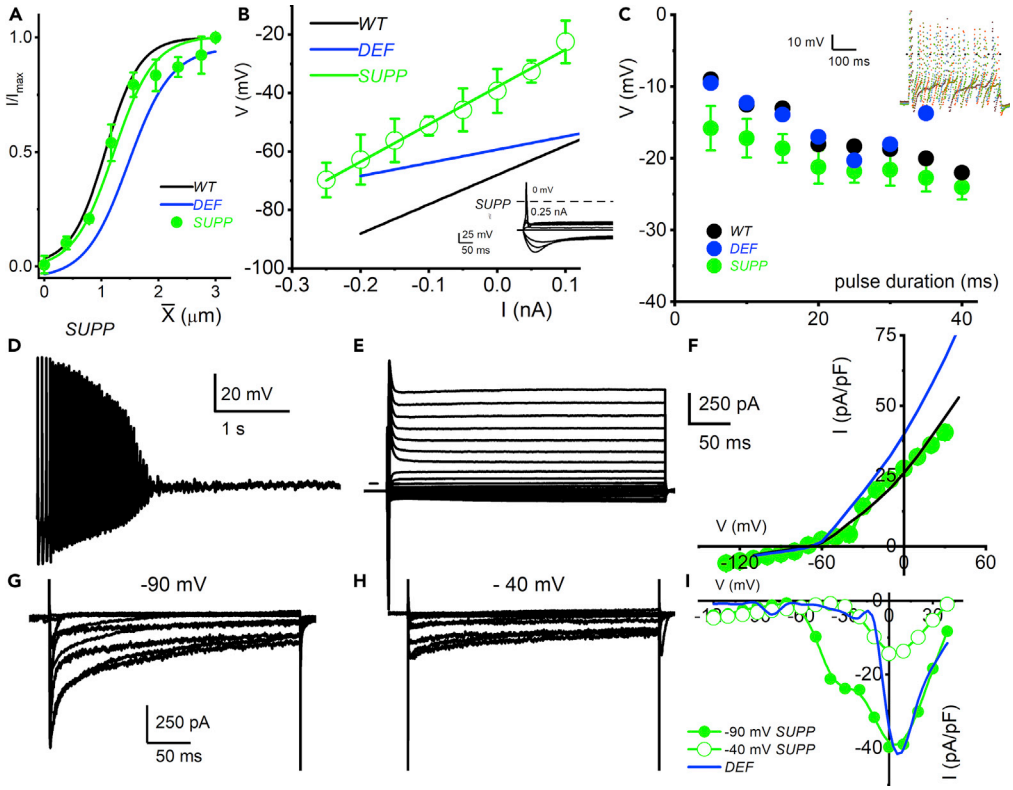

Figure 6. Membrane Properties of Small-Diameter Dorsal Root Ganglion Neurons (DRGNs) from SUPP Mice

(A) Current-clamp recordings were performed on DRGNs 6-month-old mice supplemented with 600 mg dL-alpha-tocopheryl/kg feed. Data were assessed from DRGNs with capacitance <15 pF. Membrane input resistance (R_i) was determined by evaluating membrane voltage changes in response to negative and positive current injection.

(B) The ohmic relations were fitted with linear regression and the R_i derived from the slope. SUPP mice fast-adapting DRGNs had a mean R_i of 115 ± 9 MW (n = 11).

(C) Similar to WT DRGNs, as the pulse duration was prolonged, the threshold voltage declined.

(D) Typical voltage response from slow-adapting DRGNs recorded from SUPP mice. Compared with WT DRGNs, the slow-adapting neurons in SUPP did not recover fully despite vitE supplementation.

(E)Whole-cell onward K^+ currents were elicited using depolarizing steps from −130 to 30 mV (ΔV = 10 mV), from a holding potential of −90 mV. The tail currents were at −60 mV. Current traces recorded from SUPP DRGNs are shown.

(F) Summary of steady-state currents was normalized to individual membrane capacitance (C_m), from 6-month-old SUPP mice. Data were generated from 15 DRGNs.

(G and H) Inward Ca^{2+} currents recorded from a 10-pF DRGNs in SUPP mice from −90 and −40 mV holding potentials. Currents were generated using voltage steps ranging from −120 to 40 mV.

(I) The current-voltage relations generated at −90 mV and −40 mV holding potential is plotted. The I-V relations of Ca^{2+} currents from DEF DRGNs from Figure 5E is re-plotted in blue for comparison.

Upregulation of Pro-apoptotic Transcripts with vitE Deficiency

Based on previous studies (Finno et al., 2018), evidence exists for increased apoptosis in the DRGNs with vitE deficiency by 1 year of age in DEF mice. In both the TH2 (P_{FDR} = 1.13 x 10^{-4}) and NP1 (P_{FDR} = 0.01) DRGN subpopulations, apoptosis-inducing factor, mitochondrion-associated 3 (*Aifm3*), was upregulated with vitE deficiency (WT vs. DEF and SUPP vs. DEF; Figure S4A). Additionally, tumor necrosis factor receptor superfamily, member 21 (*Tnfrsf21*), which promotes apoptosis by release of cytochrome *c* from the mitochondria into the cytoplasm, was significantly upregulated in the NP2 (P_{FDR} = 2 x 10^{-4}) and TH2 (P_{FDR} = 0.008) DRGN subpopulations (SUPP vs. DEF; Figure S4A). These results suggest that molecular signatures of apoptosis, most pronounced in TH+ DRGNs, occur by 6 months of age in DEF mice.

To further investigate the pathways leading to apoptosis of DRGNs with vitE deficiency by 1 year of age (Finno et al., 2018), and the potential preference for TH+ DRGNs, protein expression of total and cleaved

caspase 3, caspase 8, and caspase 9 was evaluated with both immunohistochemistry and Western blot analyses in 4-month-old mice. There was no evidence of total caspase 3, caspase 8, or caspase 9 activation (data not shown). However, a significant ($p < 0.01$) increase in cleaved caspase 3 and caspase 9, localized to TH+ DRGNs, was apparent in DEF mice (Figures S4B and S4C). There was no evidence of cleaved caspase 8 activation (Figure S4D).

Additional Transcript and Pathway Dysregulated with vitE Deficiency

In order to determine if the altered gene expression in the DEF DRGN was modulated by the vitE binding proteins *Ttpa* (Kono et al., 2013) and tocopherol binding protein (*Tap* or *Sec14l2*) (Zingg, 2015), we interrogated these transcripts in our dataset. *Ttpa* was not expressed in the DRGN dataset. *Sec14l2* was expressed in DRGNs but only differentially expressed between SUPP vs. DEF in the NP1 subpopulation (upregulated in DEF group; $P_{FDR} = 0.004$). Additionally, the scRNA-seq dataset was evaluated for genes encoding enzymes that have been previously found to directly bind to vitE, including protein kinase C (*Prkca*); PH domain and leucine-rich repeat protein phosphatase 2 (*Phlpp2*); cyclooxygenase-2 (Ptgs2); and lipoxygenases 5, 12, and 15 (*Alox5, Alox12,* and *Alox15*) (Domijan et al., 2014; Zingg, 2015). *Ptgs2, Alox5, Alox12,* and *Alox15* were not expressed in DRGN and, although *Phlpp2* was expressed, there were no differences between experimental groups in any DRGN subpopulation. *Prkca* was significantly downregulated in non-peptidergic DEF DRGN subpopulations (NP1, $P_{FDR} = 0.01$; NP2, $P_{FDR} = 0.001$; and NP3, $P_{FDR} = 0.03$) and upregulated in TH+ DRGN subpopulations (TH1, $P_{FDR} = 0.03$ and TH2, $P_{FDR} = 0.002$) when comparing SUPP vs. DEF.

With severe vitE deficiency, degenerative axons are identified within the caudal medulla oblongata and spinal cord with AVED (Yokota et al., 2000). Therefore, we interrogated our dataset for dysregulation of transcripts associated with axonal guidance, synaptic plasticity, and myelination. When SUPP were compared with the DEF groups, upregulation of associated transcripts was identified across DRGN subpopulations, with most transcripts upregulated in TH2 DRGNs (Table S6). Myelin basic protein (*Mbp*) was upregulated in 4/13 SUPP vs. DEF DRGNs (Table S4) but was only downregulated in the TH2 subpopulation ($P_{FDR} = 0.004$).

Because Ca^{2+} signaling triggers growth cone development during neurodevelopment (Chilton, 2006), transcripts associated with Ca^{2+} binding were interrogated in our scRNA-seq dataset. Most Ca^{2+} binding transcripts were most upregulated in TH+ DRGNs with increasing vitE deficiency (Figure S5A, contrast "C").

To further investigate the transcripts expressed among DRGN subtypes and across vitE diet groups, pathway analyses were performed using Panther Pathway overrepresentation analysis (http://pantherdb.org/). When WT and SUPP were compared with the DEF groups, the most commonly dysregulated pathways were upregulation of both the heterotrimeric G-protein signaling pathways $G_i\alpha$ and $G_s\alpha$ (P00026) and $G_q\alpha$ and $G_o\alpha$ (P00027) (Figures S5B andS5C). Significant ($P_{FDR} < 0.05$) upregulation of these two G-protein signaling pathways was identified in 9/13 DRG clusters (Table S7, Figure S6). For many of these analyses, G-protein coupled receptor (GPCR) pathways were also significantly ($P_{FDR} < 0.05$) overrepresented (Table S7).

To further investigate the potential role of enhanced G-protein signaling with vitE deficiency in specific DRGN subpopulations, specific somatosensory genes were evaluated, including G-coupled receptors (GPCRs) and the transient receptor potential vanilloid 1 (*Trpv1*) channel, as recently reviewed (Yudin and Rohacs, 2018). Associated transcripts were most significantly upregulated in TH+ expressing neurons in the SUPP vs. WT contrast (Figure S5D). These results indicate a positive association between G-protein-coupled receptor transcripts and vitE deficiency, especially in TH+ DRGNs.

Transcripts for GO-Slim biologic processes known to regulate mitochondrial functions were significantly ($P_{FDR} < 0.05$) downregulated in TH+ and NP1 DRG subpopulations (Table S7). This discovery prompted further evaluation of transcripts associated with oxidative phosphorylation. Between 30% and 50% of the transcript of mitochondrial complex I, NADH:ubiquinone oxidoreductase supernumerary subunits (NDUF) were significantly downregulated ($P_{FDR} < 0.05$) in NP1 and TH2 DRG subpopulations with vitE deficiency (Figure S5E, Table S8).

DISCUSSION

Although the antioxidant role of vitE is well established, with evidence to support protection of critical fatty acids during development of the nervous system (Miller et al., 2012; Lebold et al., 2013), the proposed

non-antioxidant roles for this vitamin remain unclear (Gohil et al., 2010; Azzi, 2007). Additionally, it remains unclear why, although all central nervous system tissues are α-TOH deficient in the *Ttpa*$^{-/-}$ mouse model, the primary clinicopathologic lesions are localized to sensory tracts. Based on the phenotype associated with AVED (Gotoda et al., 1995; Yokota et al., 1996) and recapitulated in the *Ttpa*$^{-/-}$ mouse model (Yokota et al., 2001; Finno et al., 2018), we expected a profound shift in the transcriptomic profile of the proprioceptive DRGN subpopulation. Unexpectedly, we instead identified the most pronounced message alterations in NP1 and TH+ DRGNs, responsible for mechanosensation. Both NP1 and TH+ DRGNs are small to medium in diameter and unmyelinated, whereas proprioceptive DRGNs are large-diameter myelinated neurons. Intriguingly, both NP1 and TH+ subpopulations of DRGNs arise from the same developmental lineage for C-fibers, separating into distinct lineages by E16.5–17.5 in the mouse (reviewed in Olson et al., 2016).

Upregulation of intermediate voltage-gated Ca^{2+} and K^+ channels in SUPP vs. DEF groups (Figure 2) prioritized the TH+ DRGN subpopulation for further evaluation. Within TH+ DRGNs, Ca^{2+} dysfunction with vitE deficiency was implicated by upregulation of the $Ca_v2.3$ (*Cacna1e*) and the Ca^{2+}-activated K^+ channel subunit *Kcnmb2* (Figure 3). These findings, in combination with decreased IP_3R1 (Figure S3A) and upregulation of G_q-coupled receptor pathways responsible for the formation of inositol 1,4,5 triphosphate (IP_3) (Figures S5B and S5C) in DEF mice, indicate that abnormal Ca^{2+} dynamics in TH+ DRGNs may be central to the etiology of AVED. Additionally, downregulation of Car8 (Figures 1C and S3B), a major inhibitor of IP_3R1 (Hirasawa et al., 2007; Hirota et al., 2003), indicated coordinated transcriptional changes that could contribute to overactive Ca^{2+} signaling in TH+ DRGNs. Consistent with this interpretation was the observation that acute vitE deficiency (4–6 months) reduced membrane excitability (Figures 4 and 5) and caspase activation (Figure S4), whereas long-term deficiency resulted in apoptosis of DRGNs (Finno et al., 2018). Supplementation with high-dose α-TOH in DEF mice at weaning prevented the transcriptomic and biochemical profiles described, partially prevented the electrophysiological abnormalities of TH+ DRGNs, and significantly improved mechanical sensitivity as assessed from the displacement-response curves (Figure 6A) and via the von Frey filament assay (Figure 3F). As peripheral neuropathy is a clinical feature of AVED (Gotoda et al., 1995; Fogel and Perlman, 2007), altered Ca^{2+} signaling within mechanosensitive DRGNs could provide a mechanism for loss of peripheral sensation.

Collectively, our findings are the first to link TH+ DRGNs with vitE deficiency and AVED. TH+ DRGNs constitute approximately 10%–15% of all mouse lumbar DRGNs (Brumovsky et al., 2006); are located in haired skin; and are responsive to brush, pressure, and pinch but not temperature (Li et al., 2016). In patients with AVED, loss of vibration sense and sensitivity to light touch are the frequently reported symptoms (Gotoda et al., 1995), as the dorsal column medial lemniscal neuroanatomic tract is targeted in vitE deficiency (Finno et al., 2018; Yokota et al., 1996). Therefore, we postulate that these symptoms may be due to impaired excitability and abnormal Ca^{2+} signaling. Specifically, reduced membrane excitability of mechanosensitive DRGNs could account for the peripheral neuropathy associated with AVED. Supplemental α-TOH has been demonstrated to improve peripheral neuropathy in AVED patients (Martinello et al., 1998).

Our findings identify altered Ca^{2+} signaling in TH+ DRGNs with vitE deficiency, in particular, IP_3R1 pathways. Upregulation of Ca^{2+}-binding transcripts, the voltage-gated $Ca_v2.3$ (*Cacna1e*) channel, and Ca^{2+}-activated K^+ channel subunit *Kcnmb2* are likely mechanistically interrelated alterations that further contribute to the neuropathology in TH+ DRGNs. First, electrophysiological recordings showed enhanced K^+ and Ca^{2+} current densities in small-diameter DRGNs isolated from DEF mice. Second, upregulation of GPCRs and downregulation of *Car8* support a role of altered GPCR/phospholipase C (PLC)/inositol triphosphate (IP_3) signaling in vitE-deficient TH+ DRGNs. Reactive oxygen species can activate G_q-coupled receptors, catalyzing the conversion of plasma membrane phospholipid phosphatidylinositol 4,5-bisphosphate (PIP_2) by PLC to the intracellular secondary molecules IP_3 and diacylglycerol (DAG) (Servitja et al., 2000; Vaarmann et al., 2010). As vitE remains the most potent inhibitor of lipid peroxidation (Choi et al., 2015; McDougall et al., 2017; Niki, 2014), the protection afforded at the plasma membrane may affect GPCR signaling. The decrease in small-diameter DRGN membrane excitability of DEF mice may, therefore, result from altered Ca^{2+} signaling in TH+ DRGNs. In keeping with reduced excitability of DEF DRGNs, the rate of change of membrane voltage at the upstroke phase of APs (dV/dt) was shallow compared with WT neurons (Figure 4C), which may implicate alterations in Na^+ current

magnitude and kinetics (Han et al., 2012). Although there were no significantly dysregulated Na^+ channel transcripts in the TH+ DRGNs (Table S4), posttranslational modifications of Na^+ channels may have occurred. Additionally, we cannot determine from this study if the observed effects on membrane excitability are the result of the observed gene expression changes following vitE deficiency or the insufficient vitE concentrations in the DRGNs. Experiments requiring the addition of exogenous α-TOH to DRGNs from DEF mice would be required to determine if membrane excitability can be restored with the addition of vitE. Despite this inability to definitively determine causality, the clinical relevance of these findings indicate that gene expression and membrane excitability changes within the DRGN may underlie the peripheral neuropathy observed with AVED.

By 12 months of age, apoptosis within most large- and small-diameter DRGNs is evident in DEF mice (Finno et al., 2018). Increased TUNEL staining of DRGNs in DEF mice is not observed by 6 months of age (unpublished results). In this study, scRNA-sequencing was performed only on viable cells (see ***Cell count/viability and RNA quality assurance***). Therefore, within the 6-month DEF mice examined in this study, increased activity of cleaved caspase-3 and -9 in DEF TH+ DRGNs is likely a proximal mechanism of promoting apoptosis.

Using whole tissue spinal cord homogenate, we previously identified altered nuclear receptor activation in DEF mice as they aged from weaning to 6 months (Finno et al., 2018). With sufficient vitE, retinoid orphan-related receptor alpha (RORA)-targeted transcripts were activated in the spinal cord, whereas insufficient vitE led to the activation of liver X receptor (LXR)-targeted transcripts. This effect was not observed in whole-tissue spinal cord when simply comparing groups at 6 months of age (WT vs. DEF vs. SUPP). Similarly, we did not identify upregulation of most previously investigated (Finno et al., 2018) RORA-targeted transcripts in the DRGNs between SUPP and DEF groups at 6 months of age in this current study. Comparison of DRGNs subpopulations in WT, DEF, and SUPP experimental groups between weaning and 6 months of age requires further investigation to fully elucidate the role for RORA with vitE deficiency.

Elevations in 7-oxygenated cholesterol products have been previously described in both the *Ttpa*$^{-/-}$ (Finno et al., 2018) and atherosclerotic apolipoprotein vitE-deficient mouse models (Rosenblat and Aviram, 2002). Both 7α-hydroxycholesterol and 7-ketocholesterol are inverse agonists for the constitutively active RORA (Wang et al., 2010). Therefore, we surmise that increased oxysterols suppress constitutive RORA signaling during vitE deficiency, a hypothesis that has been supported by other studies in both the *Ttpa*$^{-/-}$ mouse (Gohil et al., 2003, 2004) and the vitE-deficient horse (Finno et al., 2016). RORA activation is required for synaptic maintenance (Landis and Sidman, 1978; Sotelo and Changeux, 1974) and the neuroprotective effect is mediated by the antioxidant proteins glutathione peroxidase 1 and peroxiredoxin 6 (Boukhtouche et al., 2006). Of note, RORA controls the expression of IP_3R1 (Gold et al., 2003; Sarachana and Hu, 2013). Therefore, the underlying molecular mechanism whereby vitE deficiency leads to AVED may involve differential nuclear receptor activation with age, leading to altered IP_3R1 signaling in TH+ DRGNs, in addition to alterations in redox status at the plasma membrane (Figure 7). Alternatively, specific oxidized polyunsaturated fatty-acid-derived lipid mediators, which are protected by vitE from oxidation and destruction (Choi et al., 2015; Lebold et al., 2013; Lebold and Traber, 2014; Ulatowski and Manor, 2013), may be involved in this protective mechanism.

Single-cell RNA-seq generated a total of 382 million reads in our study, with an average of 3,614 DRGNs profiled per mouse (i.e. 7,228 neurons per experimental group). In the pioneer scRNA-seq study of DRG, pooled lumbar DRG were used to generate 2.76 billion reads across 622 single mouse neurons (Usoskin et al., 2015). A total of 3,574 ± 2,010 distinct genes were identified in each cell (Usoskin et al., 2015), as compared with our study of 1,788 ± 283 genes per cell. A subsequent publication used neuron-size-based hierarchical clustering and high-coverage scRNA-seq of 203 neurons collected from lumbar DRG of five pooled male mice (10,950 ± 1,218 genes per neuron) (Li et al., 2016). Despite the overall lower depth of sequencing across genes in our study, we were able to identify the previously characterized (Usoskin et al., 2015) neuronal subpopulations within the DRG. Previous reports (Usoskin et al., 2015; Li et al., 2016) clustered the unmyelinated TH+ neuronal population into one population. In our dataset, two distinct TH+ subgroups (TH1 and TH2) were identified across all samples. Despite highly overlapping transcriptional profiles, these subtypes were not closely enough related to merge, unlike the PEP1 subpopulation (i.e. Clusters 0 and 2). The distinct sub-clustering of TH+ subpopulations in our study warrants further investigation, as the most profound alterations with vitE deficiency in our model occurred primarily in the

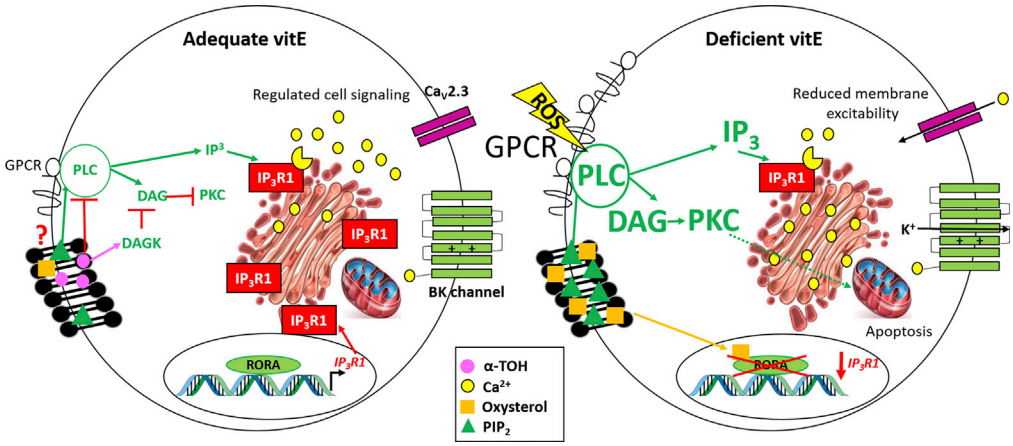

Figure 7. Proposed Mechanism of Action for α-TOH in TH+ DRGN

With adequate α-TOH (left), constitutive activity of the RAR-related orphan receptor alpha (RORA) transcription factor is maintained, increasing IP_3R1 transcription (Gold et al., 2003; Sarachana and Hu, 2013). Although there is evidence that vitE can affect the plasma membrane structure and bind to signaling enzymes to affect their activity (Zingg, 2015; Habermehl et al., 2005), we propose in this model that signaling through the PLC/IP_3/IP_3R1 axis maintains Ca^{2+} homeostasis. VitE can suppress PLC activity (Domijan et al., 2014) and, by stimulating DAGK (Koya et al., 1997), DAG is removed and PKC inhibited, providing a protective effect. With α-TOH deficiency (right), cholesterol is oxidized and resulting oxysterols repress constitutive RORA activity (Wang et al., 2010), leading to decreased IP_3R1 transcription. ROS activate the PLC/IP_3/IP_3R1 axis (Servitja et al., 2000; Vaarmann et al., 2010); however, without sufficient IP_3R1, $[Ca^{2+}]_i$ cannot increase. Additionally, loss of DAGK stimulation increases DAG and PKC. We propose this leads to the identified alterations in membrane excitability and activation of apoptotic pathways in DRGNs. BK= big potassium channel; DAG = diaglycerol; DAGK= diaglycerol kinase; IP_3 = inositol triphosphate; IP_3R1 = inositol 1,4,5 triphosphate receptor 1; PIP_2 = phosphatidylinositol 4,5-bisphosphate; PKC = protein kinase C; PLC = phospholipase C; RORA= RAR-related orphan receptor alpha; ROS = reactive oxygen species.

TH2 subpopulation. Our mice were 6 months of age, older than those used in previously reported scRNA-seq profiling studies in DRG (Li et al., 2016; Usoskin et al., 2015).

The von Frey filament assay is used on glabrous skin, which is innervated by both alpha and beta low-threshold mechanoreceptors, both not TH+ C-low threshold mechanoreceptors (Li et al., 2011). However, it has been observed that von Frey filament can activate sensitized non-peptidergic type C nociceptive fibers (i.e. NP1 subpopulations) under certain conditions (Pinto et al., 2019). In our study, the NP1 subpopulation, responsible for neuropathic pain, was also notably implicated with vitE deficiency. VitE has been demonstrated to act as an analgesic in rodent models of neuropathic pain (Kim et al., 2006), although a more recent study suggests that vitC is required concurrently (Lu et al., 2011). Foot withdrawal thresholds in response to mechanical stimuli were used to assess neuropathic pain followed by spinal cord ligation, with increased thresholds for 6 h after vitE injection (Kim et al., 2006). As neurobehavioral assays through tactile stimuli cannot reliably differentiate different DRGN activities (Li et al., 2011), we elected to document electrophysiological dysfunction in TH+-specific mechanosensitive DRGNs with vitE deficiency using whole-cell membrane recordings specific to small-diameter mechanosensitive DRGNs. However, further investigation into the role of vitE in NP1 nociceptive DRGNs is warranted.

One of the most notable findings identified in the DEF mouse model is the complete prevention of the clinical and histologic phenotype with high-dose α-TOH supplementation at weaning (Finno et al., 2018; Yokota et al., 2001). To further support these clinical findings, we have now demonstrated complete prevention of the transcriptomic and partial rescue of the electrophysiologic dysfunction within the DRGNs at the single-cell level. VitE supplementation in *Ttpa*$^{-/-}$ mice suffices to partially restore K^+ and Ca^{2+} current properties in small-diameter mechanosensitive DRGNs, but it remains unclear why slow-adapting DRGNs are impervious to vitE supplementation. Of note, α-TOH concentrations in the brain of these SUPP mice are still significantly lower than those of WT mice (Finno et al., 2018; Yokota et al., 2001), indicating that α-TTP in the brain functions in maintaining local concentration of α-TOH. Despite the lower brain α-TOH concentrations in SUPP mice compared with WT mice, the AVED clinicohistologic phenotype is completely

prevented. Therefore, a minimum concentration of vitE is likely required at this critical time in postnatal development. Even more important is the fact that the phenotype is rescuable when vitE is provided at P21, a time point that is considered the end of postnatal development in the mouse. Therefore, it may be possible that synaptogenesis and axonal elongation continue into adulthood, thereby requiring sufficient vitE from 1–6 months of age in mice.

Although this study focused on DRGNs, vitE has been demonstrated to have effects in other regions of the nervous system. Within the hippocampus, α-TOH induced long-term potentiation (Xie and Sastry, 1993), which is involved in learning and memory (Thompson, 1986). The action of vitE in hippocampal CA1 neurons occurred without a significant alteration in the membrane potential and the input resistance. Rats that are fed a vitE-deficient diet for three months had impaired long-term potential induction, with a reduction in post-tetanic potentiation, suggesting that either neurotransmitter release or postsynaptic mechanisms are involved (Xie and Sastry, 1995). It remains to be determined if the postulated mechanism for the neuroprotective effect of vitE in the DRG (Figure 7) is applicable to other regions of the nervous system.

In conclusion, we have identified the most profound transcriptomic, biochemical, and electrophysiologic changes in small-diameter TH+ mechanosensitive DRGNs, rather than the proprioceptive subpopulation, with vitE deficiency. Increased upregulation of voltage-gated Ca^{2+} and K^{+} channels led to AP abbreviation and reduced membrane excitability in TH+ DRGNs. Concurrently, alterations in IP_3R1 expression were identified, in addition to evidence of apoptosis via caspase-3- and caspase-9-mediated pathways. A highly supplemented α-TOH diet rescues the cellular and molecular alterations and represses the loss of mechanosensation found in DEF mice. The peripheral neuropathy associated with AVED likely encompasses defects in membrane properties and Ca^{2+} signaling in mechanosensitive TH+ DRGNs, providing targets for therapeutic intervention.

Limitations of the Study

We cannot determine from this study if the observed effects on membrane excitability are the result of the observed gene expression changes following vitE deficiency or the insufficient vitE concentrations in the DRGNs. Experiments requiring the addition of exogenous α-TOH to DRGNs from DEF mice would be required to determine if membrane excitability can be restored with the addition of vitE.

METHODS

All methods can be found in the accompanying Transparent Methods supplemental file.

SUPPLEMENTAL INFORMATION

Supplemental Information can be found online at https://doi.org/10.1016/j.isci.2019.10.064.

ACKNOWLEDGMENTS

Support for this work was provided by the National Institutes of Health (NIH) to C.J.F. (K01OD015134 and L40 TR001136). ENY was supported by (NIH: AG051443, DC015135, AG060504, and DC016099). Support for sequencing was provided by the University of California Davis Genome Center. We thank Dr. Isaac Pessah for his careful review of this manuscript.

AUTHOR CONTRIBUTIONS

CJF and ENY were responsible for the conceptualization, funding acquisition, methodology, investigation, formal analysis, resources, and writing of the manuscript. J.P., M.K., S.P., M.H.B., M.P.F., and J.H.L. contributed to the study and analysis of results, and B.D.J. and M.S. contributed to the informatics methodology and analysis of results. All authors have reviewed the final manuscript.

DECLARATION OF INTERESTS

The authors declare no competing financial interests.

Received: July 22, 2019
Revised: September 16, 2019
Accepted: October 28, 2019
Published: November 22, 2019

REFERENCES

Aparicio, J.M., Belanger-Quintana, A., Suarez, L., Mayo, D., Benitez, J., Diaz, M., and Escobar, H. (2001). Ataxia with isolated vitamin E deficiency: case report and review of the literature. J. Pediatr. Gastroenterol. Nutr. *33*, 206–210.

Azzi, A. (2007). Molecular mechanism of alpha-tocopherol action. Free Radic. Biol. Med. *43*, 16–21.

Azzi, A. (2018). Many tocopherols, one vitamin E. Mol. Aspects Med. *61*, 92–103.

Bellayou, H., Dehbi, H., Bourezgui, M., Slassi, I., and Nadifi, S. (2009). Ataxia with vitamin E deficiency (AVED); an example of the contribution of research in molecular genetic to counselling in Morocco. Pathol. Biol. (Paris) *57*, 425–426.

Boland, L.M., and Dingledine, R. (1990). Multiple components of both transient and sustained barium currents in a rat dorsal root ganglion cell line. J. Physiol. *420*, 223–245.

Boukhtouche, F., Vodjdani, G., Jarvis, C.I., Bakouche, J., Staels, B., Mallet, J., Mariani, J., Lemaigre-Dubreuil, Y., and Brugg, B. (2006). Human retinoic acid receptor-related orphan receptor alpha1 overexpression protects neurones against oxidative stress-induced apoptosis. J. Neurochem. *96*, 1778–1789.

Bridge, K.E., Berg, N., Adalbert, R., Babetto, E., Dias, T., Spillantini, M.G., Ribchester, R.R., and Coleman, M.P. (2009). Late onset distal axonal swelling in YFP-H transgenic mice. Neurobiol. Aging *30*, 309–321.

Brigelius-Flohe, R., and Traber, M.G. (1999). Vitamin E: function and metabolism. FASEB J. *13*, 1145–1155.

Brumovsky, P., Villar, M.J., and Hokfelt, T. (2006). Tyrosine hydroxylase is expressed in a subpopulation of small dorsal root ganglion neurons in the adult mouse. Exp. Neurol. *200*, 153–165.

Catterall, W.A., Perez-Reyes, E., Snutch, T.P., and Striessnig, J. (2005). International Union of Pharmacology. XLVIII. Nomenclature and structure-function relationships of voltage-gated calcium channels. Pharmacol. Rev. *57*, 411–425.

Cavalier, L., Ouahchi, K., Kayden, H.J., Di Donato, S., Reutenauer, L., Mandel, J.L., and Koenig, M. (1998). Ataxia with isolated vitamin E deficiency: heterogeneity of mutations and phenotypic variability in a large number of families. Am. J. Hum. Genet. *62*, 301–310.

Chilton, J.K. (2006). Molecular mechanisms of axon guidance. Dev. Biol. *292*, 13–24.

Choi, J., Leonard, S.W., Kasper, K., McDougall, M., Stevens, J.F., Tanguay, R.L., and Traber, M.G. (2015). Novel function of vitamin E in regulation of zebrafish (Danio rerio) brain lysophospholipids discovered using lipidomics. J. Lipid Res. *56*, 1182–1190.

Di Donato, I., Bianchi, S., and Federico, A. (2010). Ataxia with vitamin E deficiency: update of molecular diagnosis. Neurol. Sci. *31*, 511–515.

Domijan, A.M., Kovac, S., and Abramov, A.Y. (2014). Lipid peroxidation is essential for phospholipase C activity and the inositol-trisphosphate-related Ca(2)(+) signal. J.Cell Sci. *127*, 21–26.

Ferland, R.J., Cherry, T.J., Preware, P.O., Morrisey, E.E., and Walsh, C.A. (2003). Characterization of Foxp2 and Foxp1 mRNA and protein in the developing and mature brain. J. Comp. Neurol. *460*, 266–279.

Finno, C.J., Bordbari, M.H., Gianino, G., Ming-Whitfield, B., Burns, E., Merkel, J., Britton, M., Durbin-Johnson, B., Sloma, E.A., McMackin, M., et al. (2018). An innate immune response and altered nuclear receptor activation defines the spinal cord transcriptome during alpha-tocopherol deficiency in Ttpa-null mice. Free Radic. Biol. Med. *120*, 289–302.

Finno, C.J., Bordbari, M.H., Valberg, S.J., Lee, D., Herron, J., Hines, K., Monsour, T., Scott, E., Bannasch, D.L., Mickelson, J., and Xu, L. (2016). Transcriptome profiling of equine vitamin E deficient neuroaxonal dystrophy identifies upregulation of liver X receptor target genes. Free Radic. Biol. Med. *101*, 261–271.

Fogel, B.L., and Perlman, S. (2007). Clinical features and molecular genetics of autosomal recessive cerebellar ataxias. Lancet Neurol. *6*, 245–257.

Fukui, K., Nakamura, K., Shirai, M., Hirano, A., Takatsu, H., and Urano, S. (2015). Long-term vitamin E-deficient mice exhibit cognitive dysfunction via elevation of brain oxidation. J. Nutr. Sci. Vitaminol. (Tokyo) *61*, 362–368.

Fulgoni, V.L., 3rd, Keast, D.R., Bailey, R.L., and Dwyer, J. (2011). Foods, fortificants, and supplements: where do Americans get their nutrients? J. Nutr. *141*, 1847–1854.

Gohil, K., Godzdanker, R., O'Roark, E., Schock, B.C., Kaini, R.R., Packer, L., Cross, C.E., and Traber, M.G. (2004). Alpha-tocopherol transfer protein deficiency in mice causes multi-organ deregulation of gene networks and behavioral deficits with age. Ann. N Y Acad. Sci. *1031*, 109–126.

Gohil, K., Schock, B.C., Chakraborty, A.A., Terasawa, Y., Raber, J., Farese, R.V., Jr., Packer, L., Cross, C.E., and Traber, M.G. (2003). Gene expression profile of oxidant stress and neurodegeneration in transgenic mice deficient in alpha-tocopherol transfer protein. Free Radic. Biol. Med. *35*, 1343–1354.

Gohil, K., Vasu, V.T., and Cross, C.E. (2010). Dietary alpha-tocopherol and neuromuscular health: search for optimal dose and molecular mechanisms continues! Mol. Nutr. Food Res. *54*, 693–709.

Gold, D.A., Baek, S.H., Schork, N.J., Rose, D.W., Larsen, D.D., Sachs, B.D., Rosenfeld, M.G., and Hamilton, B.A. (2003). RORalpha coordinates reciprocal signaling in cerebellar development through sonic hedgehog and calcium-dependent pathways. Neuron *40*, 1119–1131.

Gotoda, T., Arita, M., Arai, H., Inoue, K., Yokota, T., Fukuo, Y., Yazaki, Y., and Yamada, N. (1995). Adult-onset spinocerebellar dysfunction caused by a mutation in the gene for the alpha-tocopherol-transfer protein. N. Engl. J. Med. *333*, 1313–1318.

Habermehl, D., Kempna, P., Azzi, A., and Zingg, J.M. (2005). Recombinant SEC14-like proteins (TAP) possess GTPase activity. Biochem. Biophys. Res. Commun. *326*, 254–259.

Han, C., Hoeijmakers, J.G., Liu, S., Gerrits, M.M., te Morsche, R.H., Lauria, G., Dib-Hajj, S.D., Drenth, J.P., Faber, C.G., Merkies, I.S., et al. (2012). Functional profiles of SCN9A variants in dorsal root ganglion neurons and superior cervical ganglion neurons correlate with autonomic symptoms in small fibre neuropathy. Brain *135*, 2613–2628.

Hirasawa, M., Xu, X., Trask, R.B., Maddatu, T.P., Johnson, B.A., Naggert, J.K., Nishina, P.M., and Ikeda, A. (2007). Carbonic anhydrase related protein 8 mutation results in aberrant synaptic morphology and excitatory synaptic function in the cerebellum. Mol.Cell.Neurosci. *35*, 161–170.

Hirota, J., Ando, H., Hamada, K., and Mikoshiba, K. (2003). Carbonic anhydrase-related protein is a novel binding protein for inositol 1,4,5-trisphosphate receptor type 1. Biochem. J. *372*, 435–441.

Jia, L.F., Wang, L., Chopp, M., Li, C., Zhang, Y., Szalad, A., and Zhang, Z.G. (2018). MiR-29c/PRKCI regulates axonal growth of dorsal root ganglia neurons under hyperglycemia. Mol. Neurobiol. *55*, 851–858.

Kim, H.K., Kim, J.H., Gao, X., Zhou, J.L., Lee, I., Chung, K., and Chung, J.M. (2006). Analgesic effect of vitamin E is mediated by reducing central sensitization in neuropathic pain. Pain *122*, 53–62.

Kono, N., Ohto, U., Hiramatsu, T., Urabe, M., Uchida, Y., Satow, Y., and Arai, H. (2013). Impaired alpha-TTP-PIPs interaction underlies familial vitamin E deficiency. Science *340*, 1106–1110.

Koya, D., Lee, I.K., Ishii, H., Kanoh, H., and King, G.L. (1997). Prevention of glomerular dysfunction in diabetic rats by treatment with d-alpha-tocopherol. J. Am. Soc. Nephrol. *8*, 426–435.

Landis, D.M., and Sidman, R.L. (1978). Electron microscopic analysis of postnatal histogenesis in the cerebellar cortex of staggerer mutant mice. J. Comp. Neurol. *179*, 831–863.

Lebold, K.M., Kirkwood, J.S., Taylor, A.W., Choi, J., Barton, C.L., Miller, G.W., La Du, J., Jump, D.B., Stevens, J.F., Tanguay, R.L., and Traber, M.G. (2013). Novel liquid chromatography-mass spectrometry method shows that vitamin E deficiency depletes arachidonic and docosahexaenoic acids in zebrafish (Danio rerio) embryos. Redox Biol. *2*, 105–113.

Lebold, K.M., and Traber, M.G. (2014). Interactions between alpha-tocopherol, polyunsaturated fatty acids, and lipoxygenases during embryogenesis. Free Radic. Biol. Med. *66*, 13–19.

Li, C.L., Li, K.C., Wu, D., Chen, Y., Luo, H., Zhao, J.R., Wang, S.S., Sun, M.M., Lu, Y.J., Zhong, Y.Q., et al. (2016). Somatosensory neuron types identified by high-coverage single-cell RNA-

sequencing and functional heterogeneity. Cell Res *26*, 967.

Li, L., Rutlin, M., Abraira, V.E., Cassidy, C., Kus, L., Gong, S., Jankowski, M.P., Luo, W., Heintz, N., Koerber, H.R., et al. (2011). The functional organization of cutaneous low-threshold mechanosensory neurons. Cell *147*, 1615–1627.

Lu, R., Kallenborn-Gerhardt, W., Geisslinger, G., and Schmidtko, A. (2011). Additive antinociceptive effects of a combination of vitamin C and vitamin E after peripheral nerve injury. PLoS One *6*, e29240.

Maras, J.E., Bermudez, O.I., Qiao, N., Bakun, P.J., Boody-Alter, E.L., and Tucker, K.L. (2004). Intake of alpha-tocopherol is limited among US adults. J. Am.Diet Assoc. *104*, 567–575.

Martinello, F., Fardin, P., Ottina, M., Ricchieri, G.L., Koenig, M., Cavalier, L., and Trevisan, C.P. (1998). Supplemental therapy in isolated vitamin E deficiency improves the peripheral neuropathy and prevents the progression of ataxia. J. Neurol. Sci. *156*, 177–179.

Martinov, T., Mack, M., Sykes, A., and Chatterjea, D. (2013). Measuring changes in tactile sensitivity in the hind paw of mice using an electronic von Frey apparatus. J. Vis. Exp. *82*, e51212.

McDougall, M., Choi, J., Truong, L., Tanguay, R., and Traber, M.G. (2017). Vitamin E deficiency during embryogenesis in zebrafish causes lasting metabolic and cognitive impairments despite refeeding adequate diets. Free Radic. Biol. Med. *110*, 250–260.

Institute of Medicine (2000). Dietary Reference Intakes: Vitamin C, Vitamin E, Selenium, and Carotenoids (Washington, DC: The National Academeies Press).

Miller, G.W., Ulatowski, L., Labut, E.M., Lebold, K.M., Manor, D., Atkinson, J., Barton, C.L., Tanguay, R.L., and Traber, M.G. (2012). The alpha-tocopherol transfer protein is essential for vertebrate embryogenesis. PLoS One *7*, e47402.

Muller, D.P. (2010). Vitamin E and neurological function. Mol. Nutr. Food Res. *54*, 710–718.

Nakaya, N., Sultana, A., Lee, H.S., and Tomarev, S.I. (2012). Olfactomedin 1 interacts with the Nogo a receptor complex to regulate axon growth. J. Biol. Chem. *287*, 37171–37184.

Niki, E. (2014). Role of vitamin E as a lipid-soluble peroxyl radical scavenger: in vitro and in vivo evidence. Free Radic. Biol. Med. *66*, 3–12.

Olson, W., Dong, P., Fleming, M., and Luo, W. (2016). The specification and wiring of mammalian cutaneous low-threshold mechanoreceptors. Wiley Interdiscip. Rev. Dev. Biol. *5*, 389–404.

Pinto, L.G., Souza, G.R., Kusuda, R., Lopes, A.H., Sant'Anna, M.B., Cunha, F.Q., Ferreira, S.H., and Cunha, T.M. (2019). Non-peptidergic nociceptive neurons are essential for mechanical inflammatory hypersensitivity in mice. Mol. Neurobiol. *56*, 5715–5728.

Rosenblat, M., and Aviram, M. (2002). Oxysterol-induced activation of macrophage NADPH-oxidase enhances cell-mediated oxidation of LDL in the atherosclerotic apolipoprotein E deficient mouse: inhibitory role for vitamin E. Atherosclerosis *160*, 69–80.

Sarachana, T., and Hu, V.W. (2013). Genome-wide identification of transcriptional targets of RORA reveals direct regulation of multiple genes associated with autism spectrum disorder. Mol. Autism *4*, 14.

Saunders, A., Macosko, E.Z., Wysoker, A., Goldman, M., Krienen, F.M., De Rivera, H., Bien, E., Baum, M., Bortolin, L., Wang, S.Y., et al. (2018). Molecular diversity and specializations among the cells of the adult mouse brain. Cell *174*, 1015–1030.e16.

Schuelke, M. (1993). Ataxia with vitamin E deficiency. In GeneReviews((R)), M.P. Adam, H.H. Ardinger, R.A. Pagon, S.E. Wallace, L.J.H. Bean, K. Stephens, and A. Amemiya, eds. (University of Washington).

Servitja, J.M., Masgrau, R., Pardo, R., Sarri, E., and Picatoste, F. (2000). Effects of oxidative stress on phospholipid signaling in rat cultured astrocytes and brain slices. J. Neurochem. *75*, 788–794.

Sotelo, C., and Changeux, J.P. (1974). Transsynaptic degeneration 'en cascade' in the cerebellar cortex of staggerer mutant mice. Brain Res. *67*, 519–526.

Thompson, R.F. (1986). The neurobiology of learning and memory. Science *233*, 941–947.

Traber, M.G., and Atkinson, J. (2007). Vitamin E, antioxidant and nothing more. Free Radic. Biol. Med. *43*, 4–15.

Ulatowski, L., and Manor, D. (2013). Vitamin E trafficking in neurologic health and disease. Annu. Rev. Nutr. *33*, 87–103.

Ulatowski, L., Parker, R., Warrier, G., Sultana, R., Butterfield, D.A., and Manor, D. (2014). Vitamin E is essential for Purkinje neuron integrity. Neuroscience *260*, 120–129.

Usoskin, D., Furlan, A., Islam, S., Abdo, H., Lonnerberg, P., Lou, D., Hjerling-Leffler, J., Haeggstrom, J., Kharchenko, O., Kharchenko, P.V., et al. (2015). Unbiased classification of sensory neuron types by large-scale single-cell RNA sequencing. Nat. Neurosci. *18*, 145–153.

Vaarmann, A., Gandhi, S., and Abramov, A.Y. (2010). Dopamine induces Ca2+ signaling in astrocytes through reactive oxygen species generated by monoamine oxidase. J. Biol. Chem. *285*, 25018–25023.

Wang, Y., Kumar, N., Solt, L.A., Richardson, T.I., Helvering, L.M., Crumbley, C., Garcia-Ordonez, R.D., Stayrook, K.R., Zhang, X., Novick, S., et al. (2010). Modulation of retinoic acid receptor-related orphan receptor alpha and gamma activity by 7-oxygenated sterol ligands. J. Biol. Chem. *285*, 5013–5025.

Wu, Z.Z., and Pan, H.L. (2004). High voltage-activated Ca(2+) channel currents in isolectin B(4)-positive and -negative small dorsal root ganglion neurons of rats. Neurosci. Lett. *368*, 96–101.

Xie, L., Dolai, S., Kang, Y., Liang, T., Xie, H., Qin, T., Yang, L., Chen, L., and Gaisano, H.Y. (2016). Syntaxin-3 binds and regulates both R- and L-type calcium channels in insulin-secreting INS-1 832/13 cells. PLoS One *11*, e0147862.

Xie, Z., and Sastry, B.R. (1993). Induction of hippocampal long-term potentiation by alpha-tocopherol. Brain Res. *604*, 173–179.

Xie, Z., and Sastry, B.R. (1995). Impairment of long-term potentiation in rats fed with vitamin E-deficient diet. Brain Res. *681*, 193–196.

Yokota, T., Igarashi, K., Uchihara, T., Jishage, K., Tomita, H., Inaba, A., Li, Y., Arita, M., Suzuki, H., Mizusawa, H., and Arai, H. (2001). Delayed-onset ataxia in mice lacking alpha -tocopherol transfer protein: model for neuronal degeneration caused by chronic oxidative stress. Proc. Natl. Acad. Sci. U S A *98*, 15185–15190.

Yokota, T., Shiojiri, T., Gotoda, T., and Arai, H. (1996). Retinitis pigmentosa and ataxia caused by a mutation in the gene for the alpha-tocopherol-transfer protein. N. Engl. J. Med. *335*, 1770–1771.

Yokota, T., Uchihara, T., Kumagai, J., Shiojiri, T., Pang, J.J., Arita, M., Arai, H., Hayashi, M., Kiyosawa, M., Okeda, R., and Mizusawa, H. (2000). Postmortem study of ataxia with retinitis pigmentosa by mutation of the alpha-tocopherol transfer protein gene. J. Neurol. Neurosurg. Psychiatry *68*, 521–525.

Yudin, Y., and Rohacs, T. (2018). Inhibitory G(i/O)-coupled receptors in somatosensory neurons: potential therapeutic targets for novel analgesics. Mol. Pain *14*, 1744806918763646.

Zhuang, G.Z., Keeler, B., Grant, J., Bianchi, L., Fu, E.S., Zhang, Y.P., Erasso, D.M., Cui, J.G., Wiltshire, T., Li, Q., et al. (2015). Carbonic anhydrase-8 regulates inflammatory pain by inhibiting the ITPR1-cytosolic free calcium pathway. PLoS One *10*, e0118273.

Zingg, J.M. (2015). Vitamin E: a role in signal transduction. Annu. Rev. Nutr. *35*, 135–173.

ISCI, Volume *21*

Supplemental Information

Single-Cell RNA-seq Reveals Profound Alterations in Mechanosensitive Dorsal Root Ganglion Neurons with Vitamin E Deficiency

Carrie J. Finno, Janel Peterson, Mincheol Kang, Seojin Park, Matthew H. Bordbari, Blythe Durbin-Johnson, Matthew Settles, Maria C. Perez-Flores, Jeong H. Lee, and Ebenezer N. Yamoah

Supplemental Figures

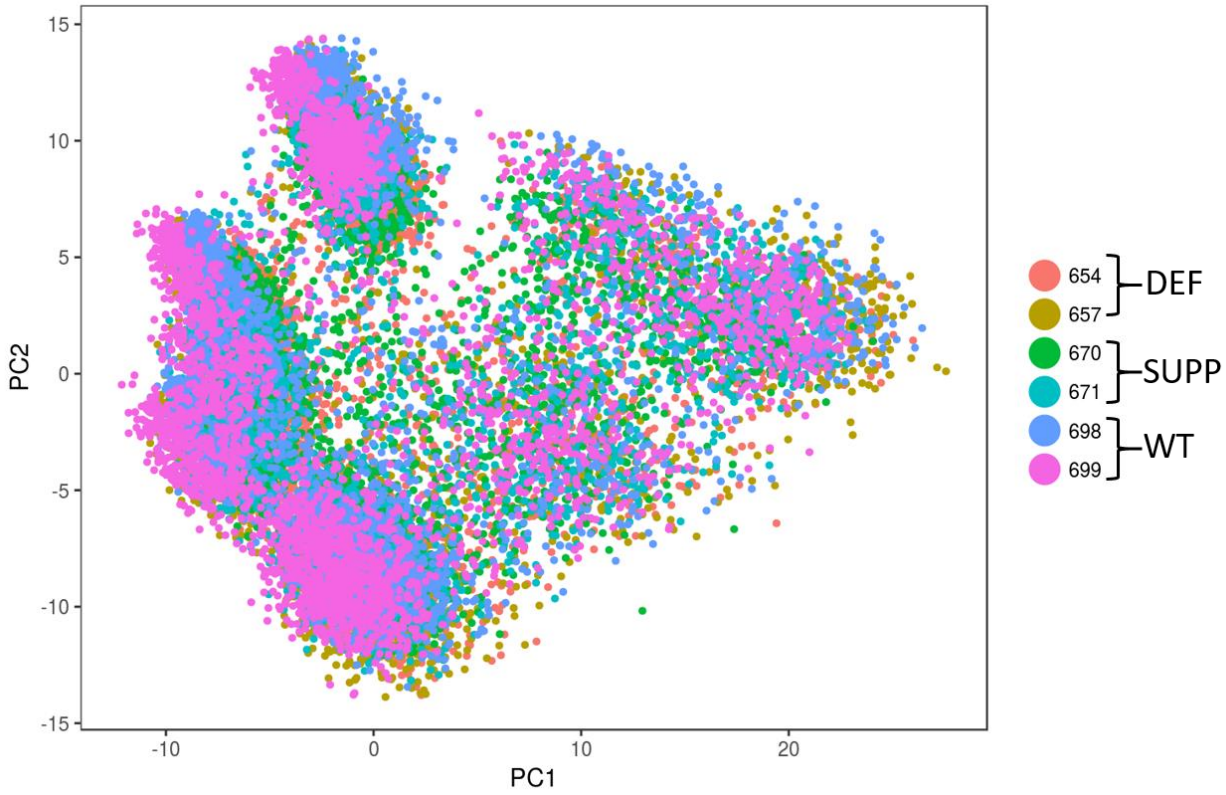

Figure S1, related to Figure 1A: Principal component analysis identified no difference in neuronal clustering between experimental groups.

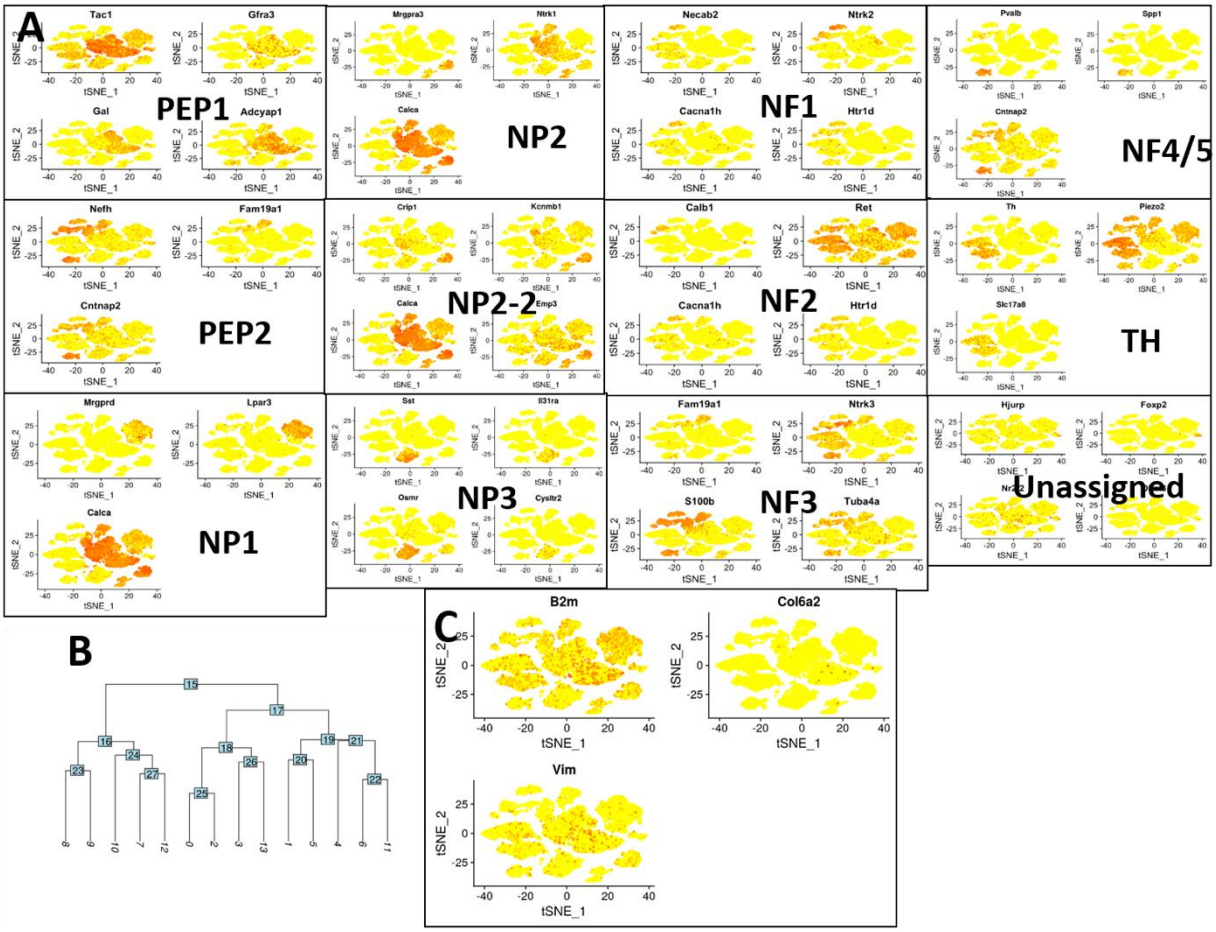

Figure S2, related to Figure 1A: (A) Classification of DRG subpopulations based on previously reported gene expression profiles (Li et al., 2016; Usoskin et al., 2015). NF=neurofilament, NP=non-peptidergic, PEP=peptidergic, TH=tyrosine hydroxylase, UNASSIGNED=unassigned cluster, n=2 mice per group with ~3,600 cells/mouse profiled. **(b)** Cluster dendogram used to determine subpopulations. Clusters 0 and 2 were merged into Cluster 0.2 based on shared peptidergic neuronal cell markers. **(C)** A distinct subpopulation of microglia cells, using previously identified transcriptional markers, was not identified in this dataset (Li et al., 2016; Usoskin et al., 2015).

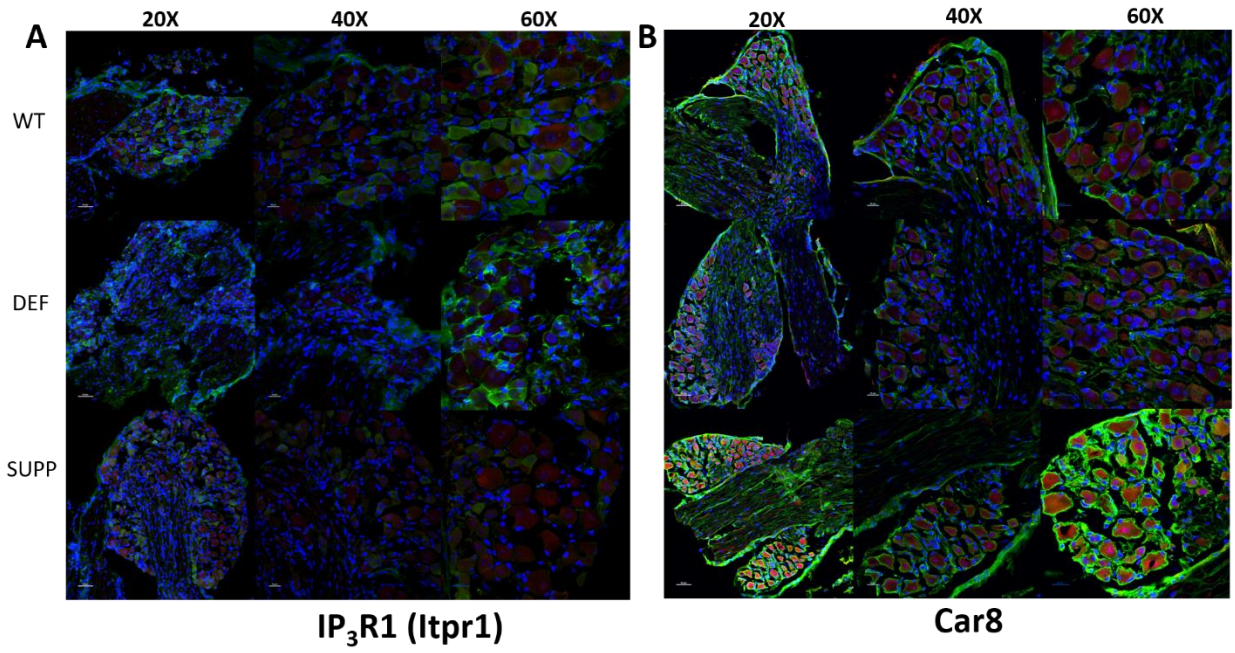

Figure S3, related to Fig. 1C: Triple-labeling identified decreased (A) IP_3R1 (Itpr1) and decreased (B) Car8 protein expression in tyrosine hydroxylase positive DRGN with vitE deficiency. Red: IP_3R1 (Itpr1) **(A)** or Car8 **(B)**; Green: Th, Blue: DAPI nuclei. Fluorescent immunohistochemistry from 4-month WT, DEF, and SUPP mice. 20x=50 μm, 40x=20 μm, 60x=20 μm

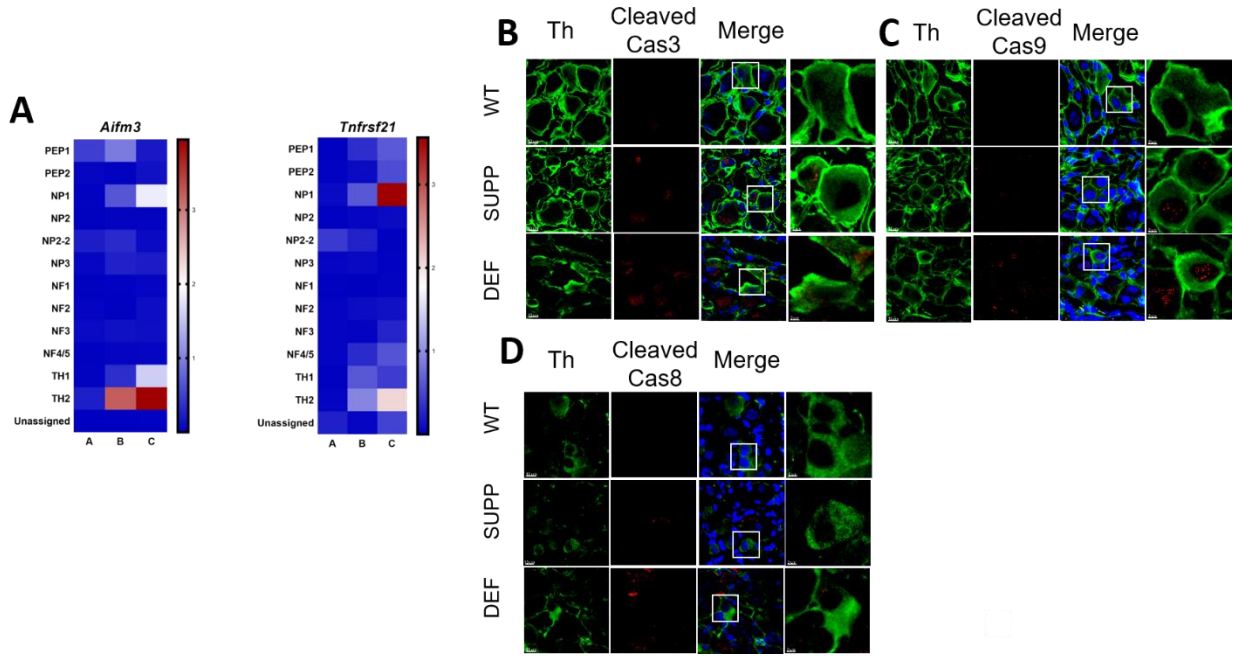

Figure S4, related to Fig. 7: Apoptosis of TH+ DRGNs with vitE deficiency. (A) Heat maps, plotted by $-\log P_{adjusted}$, comparing the degree of upregulation for apoptotic transcripts in DRGN subpopulations with α-TOH deficiency, with the most significantly upregulation in the Th2 subpopulation. Contrast A= SUPP vs. WT, contrast B= WT vs. DEF, contrast C= SUPP vs. DEF. *Aifm3*=apoptosis-inducing factor, mitochondrion-associated, *Tnfrsf21*=tumor necrosis factor receptor superfamily, member 21. Triple-labeling identified **(B)** increased cleaved caspase 3**, (C)** increased cleaved caspase 9 and **(D)** unchanged cleaved caspase 8 in TH+ DRGN with vitE deficiency. Green: Th, Blue: DAPI nuclei. Red: **(B)** Cleaved caspase 3, **(C)** Cleaved caspase 9 and **(D)** cleaved caspase 8**.** White box inset magnified in last column. Fluorescent immunohistochemistry from 4 month WT, DEF, and SUPP mice. Scale bars= 10 μm (TH, Cleaved Cas3, Cas9, Cas 8 and merge) and 3 μm (enlarged; last column).

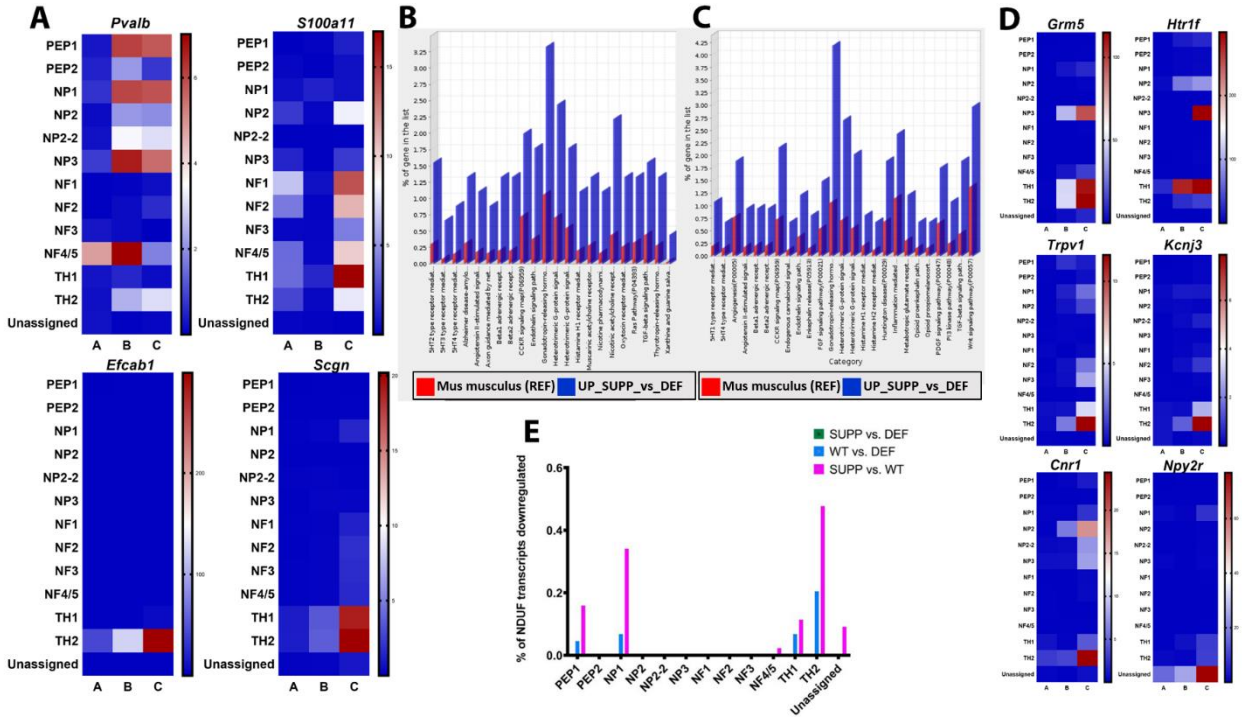

Figure S5, related to Fig. 1: Upregulation of Ca^{2+} binding transcripts and G-protein signaling pathways and downregulation of mitochondrial complex I transcripts in TH+ DRGNs with vitE deficiency. Heat maps, plotted by $-\log P_{adjusted}$, comparing the degree of upregulation for **(A)** selected Ca^{2+} binding transcripts in DRGN subpopulations with vitE deficiency. Representative Panther Pathway overrepresentation analysis (red=*Mus musculus* database, blue=overrepresented pathways of the SUPP vs WT groups) from the **(B)** TH1 and **(C)** TH2 subpopulations demonstrating upregulation of G-protein signaling pathways and G-protein coupled receptors (GPCRs). These pathways were identified as upregulated in 9/13 DRGN subpopulations (additional figures; **Figure S6**). **(D)** Heat maps, plotted by $-\log P_{adjusted}$, comparing the degree of upregulation for selected G-protein coupled receptor genes and the transient receptor potential vallinoid (*Trpv1*) channel in DRGN subpopulations with vitE deficiency. Contrast A= SUPP vs. WT, contrast B= WT vs. DEF , contrast C= SUPP vs. DEF. **(E)** Percent of mitochondrial complex I: NADH:ubiquinone oxidoreductase supernumerary subunits (NDUF) downregulated in DRGN subpopulations with α-TOH deficiency. The most pronounced downregulation was within the NP1 (34%) and TH2 (47%) subpopulations. *Cacna1e*= Cav2.3 intermediate voltage-activated Ca^{2+} channel, *Cnr1*=cannaboinoid receptor 1, *Efcab1*=EF-hand calcium binding domain 1, *Grm*=metabotropic glutamate receptor 5, *Hrt1f*=5HT receptor 1f, *Kcnj3*= GIRK1, *Kcnmb*=Potassium large conductance calcium-activated channel, subfamily M, beta, *Npy2r*=NPY receptor 2, *Pvalb*=parvalbumin, *S100a11*=S100 calcium-binding protein A11, *Scgn*=secretagogin.

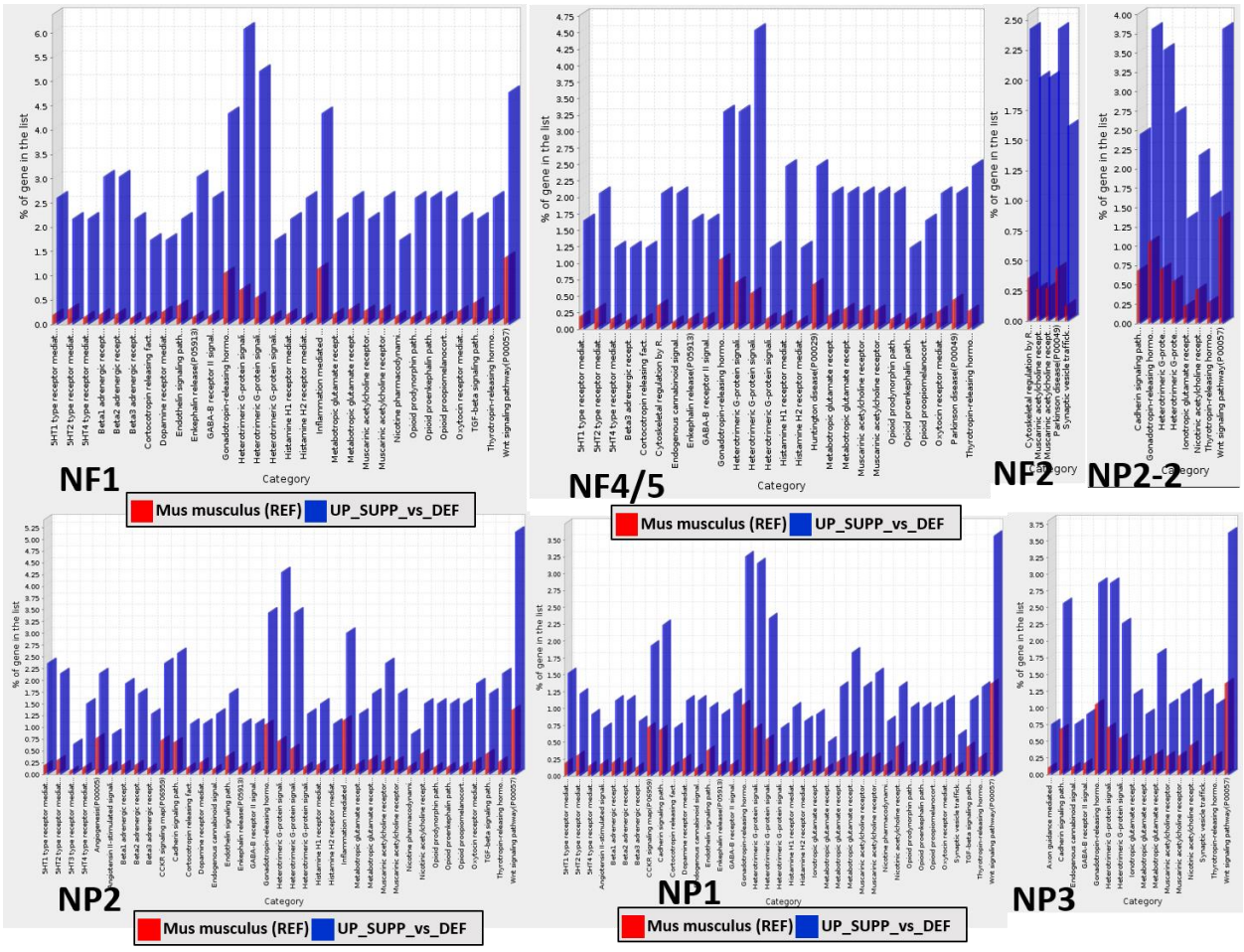

Figure S6, related to Fig. 1: Representative Panther Pathway overrepresentation analysis results of the SUPP vs DEF groups from the other DRG subpopulations, demonstrating upregulation of G-protein signaling pathways in a total of 9/13 DRG subpopulations (TH+ subpopulations in Figs 2D,E).

Supplemental Tables

Tables S1, S4 and S7 are separate Excel files due to size

Table S2, related to Fig. 1: Number/name of top genes defining each dorsal root ganglia (DRG) subpopulation			
DRG subpopulation	**# of genes defining each subpopulation**	**Median # of cells sequenced**	**Top transcripts defining neuronal subgroups**
PEP1 (peptidergic 1) Peptidergic nociception	139	1098	*Calca, Tac1, Kit, Ntrk1, Gal, Adcyap1, Gfra3*
PEP2 (peptidergic 2) Peptidergic nociception	82	141	*Ntrk1, Nefh, Cntnap2, Kit, Calca, Fam19a1*
NP1 Non-peptidergic nociception	92	465	*Mrgprd, Lpar3, Calca, Plxnc1, Scg3, Ctxn3, Gfra2*
NP2 Non-peptidergic nociception	63	102	*Mrgpra3, Ntrk1, Calca, Plxnc1, Adora2b, Cbln1*
NP2-2 Non-peptidergic nociception	25	169	*Crip1, Kcnmb1, Calca, Emp3*
NP3 Non-peptidergic nociception	187	328	*Osmr, Sst, Il31ra, Cysltr2, Nppb, Nts*
NF1 (neurofilament 1) Low threshold mechanoreceptors	72	113	*Necab2, Ntrk2, Cacna1h, Ldhb, Nefh, Htr1d*
NF2 (neurofilament 2) Low threshold mechanoreceptors	168	124	*Nefh, Ntrk2, Ntrk3, Calb1, Ldhb, Ret*
NF3 (neurofilament 3) Low threshold mechanoreceptors	59	96	*Nefh, Fam19a1, Ntrk3, Ldhb, S100b, Tuba4a*
NF4-5 (neurofilament 4-5) Proprioception	196	107	*Pvalb, Cntnap2, Spp1, Nefh, Cntnap2, Nxph1, Ldhb*
TH1 (tyrosine hydroxylase) Type C low-threshold mechanoreceptors	102	380	*Th, Piezo2, Slc17a8, Gfra2, Zfp521*
TH2 (tyrosine hydroxylase) Type C low-threshold mechanoreceptors	254	317	*Th, Piezo2, Slc17a8, Gfra2, Zfp521*
Unassigned	106	52	N/A

Table S3, related to Fig. 1: Number of differentially expressed transcripts (DETs) per DRG subpopulation within each contrast. Experimental groups defined in Transparent Methods										
		WT vs. DEF			SUPP vs. WT			SUPP vs. DEF		
Cluster#	ClusterName	#DETs	DOWNREGULATED (Panther)	UPREGULATED	#DETS	DOWNREGULATED (Panther)	UPREGULATED	#DETs	DOWNREGULATED	UPREGULATED
0.2	PEP1	228	62	166	65	14	51	465	143	322
1	NP1	463	78	385	154	56	98	1801	795	1006
3	TH1	249	33	216	95	33	62	520	64	456
4	NP3	391	75	316	92	35	57	787	113	674
5	TH2	398	77	321	122	59	63	1138	386	752
6	X	219	15	204	71	33	38	474	101	373
7	PEP2	66	11	55	21	2	19	186	34	152
8	NF2	53	10	43	48	12	36	495	231	264
9	NF4/5	54	3	51	43	9	34	343	88	255
10	NF1	114	14	100	59	12	47	314	63	251
11	NP2	273	7	266	110	42	68	535	62	473
12	NF3	88	15	72	52	7	45	333	107	226
13	Unassigned	192	22	170	100	13	87	424	44	380

Table S5, related to Fig. 2: Differentially expressed transcripts associated with Ca^{2+} and K^+ channels that passed $P_{FDR} < 0.05$ across the DRG subpopulations

		PEP1	PEP2	NP1	NP2	NP2-2	NP3	NF1	NF2	NF3	NF4/5	TH1	TH2	Un
Voltage-gated Ca^{2+} channels														
L-type ("Long-lasting")	*Cacna1c*								X			X	X	
P-type ("Purkinje")	*Cacna1a*													
N-type ("Neural"	*Cacna1b*			X										
R-type ("Residual")	*Cacna1e*			X	X	X	X	X		X	X	X	X	
Type-type ("Transient")	*Cacna1h*			X	X		X							
	Cacna1l	X		X	X	X	X		X					X
Ligand-gated Ca^{2+} channels														
IP_3 receptor	*Itpr1*													
	Itpr3													
Ryanodine receptor	*Ryr2*			X	X		X		X			X	X	
	Ryr3													
Two-pore channel	*Tpcn1*													
Cation channels of sperm	*Pkd2*													
Store-operated channels	*Orai1*													
	Orai2													
	Orai3													
K^+ channels														
Ca^{2+}-activated K^+ channels	*Kcnmb1*											X	X	
	Kcnmb2			X	X	X						X	X	
K^+ two-pore domain subfamily K	*Kcnk2*					X					X		X	
	Kcnk3			X	X							X	X	
	Kcnk12											X	X	
	Kcnk18	X	X									X	X	X
K^+ voltage-gated channel subfamily J (inward rectifying K^+ channels)	*Kncj2*			X	X	X		X				X	X	
	Kcnj3						X						X	
	Kcnj4	X		X	X		X							
K^+ voltage-gated channel	*Kcna2*			X		X	X							
	Kcnab1	X			X	X	X							
	Kcnb2											X	X	
	Kcnc1			X	X	X	X						X	
	Kcnc2			X	X	X			X	X	X			
	Kcnc4				X	X	X					X		
	Kcnd2		X	X		X	X							
	Kcnd3	X					X							
	Kcnh2			X	X		X							
	Kcnq2					X	X							
	Kcnq3	X		X			X							
	Kcnq5					X	X							
	Kcns1	X				X								X
	Kcns3										X	X	X	
	Kcnv1		X					X	X		X		X	X

Table S6, related to Fig. 1: Differentially expressed transcripts associated with synaptogeneis, axonal growth and myelination that passed $P_{FDR} < 0.05$ across the DRG subpopulations

		PEP1	PEP2	NP1	NP2	NP2-2	NP3	NF1	NF2	NF3	NF4/5	TH1	TH2	Un
Cerebellin precursor proteins synapse integrity and plasticity	*Cbln1*			X			X	X					X	
	Cbln2	X	X	X	X	X	X							
Sema domain– normal brain development, axon guidance and cell migration	*Sema4c*											X	X	
	Sema5a			X		X	X					X	X	
	Sema6a											X		
	Sema7a	X		X	X		X							
Solute carrier family 17 –uptake of glutamate at presynaptic nerve terminals	*Slc17a6*						X				X			
	Slc17a7	X		X										
	Slc17a8				X	X	X		X	X	X			
Unc-5 homology A – receptor for netrin required for axon guidance	*Unc5a*	X	X		X	X								
	Unc5b							X		X				X
	Unc5c						X					X	X	
	Unc5d			X		X				X		X	X	
	Unc13c							X					X	
Axonal growth and extension	*Bdnf* – neuronal survival and differentiation											X	X	
	Btbd3 – directs dendrites toward active axon terminals											X	X	
	Dpsyl2 - axonal guidance			X									X	
	Kif21a – kinesin family axonal transport			X									X	
	Ntrk1 – tyrosine kinase receptor involved in axonal extension			X				X	X		X	X	X	
	Rtn4r – axonal growth inhibition											X	X	
	Slit2 – axonal navigation	X		X	X	X	X			X			X	
Synaptic vesicle	*Cplx2* – complexin 2 formation of synaptic vesicle clustering			X									X	
	Stxbp6 – syntaxin binding protein	X		X	X	X	X						X	
	Sv2a – synaptic vesicle glycoprotein			X			X		X	X				
	Sv2b – synaptic vesicle glycoprotein			X	X							X	X	
	Syt3 – synaptotagmin III	X		X		X	X							
	Syt16 – synaptotagmin XVI			X		X		X					X	
	Sytl3 – synaptotagmin-like III						X	X				X	X	
Myelination	*Mbp* – myelin binding protein	X		X		X	X						X (Down)	
	Omg – Oligodendrocyte myelin glycoprotein			X	X	X						X	X	

Table S8, related to Fig. 1: Differentially expressed transcripts of the mitochondrial complex I:NADH:ubiquinone oxidoreductase supernumary subunits (NDUF)

	PEP1	PEP2	NP1	NP2	NP2-2	NP3	NF1	NF2	NF3	NF4/5	TH1	TH2	Un
Ndufa9			X									X	
Ndufa10			X										
Ndufa11	X		X									X	
Ndufa12			X									X	
Ndufa13													X
Ndufab1			X									X	
Ndufaf2												X	
Ndufaf3			X									X	
Ndufaf6			X										
Ndufaf7			X									X	
Ndufb2											X	X	
Ndufb3												X	
Ndufb4												X	
Ndufb6			X									X	
Ndufb8	X												
Ndufb9													X
Ndufb11	X												
Ndufc1	X											X	
Ndufs2			X									X	
Ndufs3												X	X
Ndufs4			X									X	
Ndufs5			X									X	
Ndufs6											X		
Ndufs7			X									X	
Ndufs8			X									X	
Ndufv1			X										
Ndufv3	X												

Transparent Methods

Contact for Reagent and Resource Sharing

Further information and requests for resources and reagents should be directed to and will be fulfilled by the Lead Contact, Carrie J. Finno (cjfinno@ucdavis.edu).

Reagents for scRNA-seq preparation

Growth medium for primary DRG cell culture consisted of five components that included: 500 mL nutrient mixture F-12 with phenol red stored at 4oC (Gibco™ Ham's F-12 Nutrient Mix), 5 mL Penicillin/Streptomycin stock (100 U/mL), 5 mL 100X N2 supplement, 10 mL 50X B-27 supplement, and 50 mL FBS (10% v/v). Stock solution (15% w/v) was prepared using 1.5 g of BSA (Sigma-Aldrich, St. Louis, MO) in 10 mL of F-12 medium. The same BSA lot number was used for WT, DEF and SUPP groups. The solution was placed in a 37°C water bath to dissolve BSA further. The F-12 medium was filter-sterilized (using a 40µm Flowmi™ Cell Strainer) and made into a final solution using a 12 mL syringe/filter. The solution was made the day of DRG cell processing. Stock solution (12.5 mg/mL; 1.25% w/v) was prepared by placing 50 mg collagenase IV in 4 mL F-12 (no phenol red) and was sterilized by a 0.22 µm filter. When resecting the DRG cells, 200 µL of collagenase IV (Gibco™ 17104019) was added to 1.8 mL HBSS (Hank's Balanced Salt Solution).

Experimental model and subject details

Mice

Animals were housed and cared for under the University of California Davis (UCD) and University of Reno (UNR) standing committee on animal use and care (IACUC) as well as the Guide for the Care and Use of Laboratory animals (8th edition, 2011). All procedures performed were also approved by the University (UCD and UNR) IACUC. A rederived colony of mixed (50% C57BL6 and 50% 129/SvJae) mice heterozygous for the deletion (*Ttpa*$^{+/-}$) were crossed with C57BL6/J (*Ttpa*$^{-/-}$) mice to establish a colony of *Ttpa*$^{-/-}$ mice. Offspring were genotyped using specific primers for *Ttpa*, and genotypes confirmed by western blot analysis of hepatic TTP using an anti-TTP antibody as previously described (Terasawa et al., 2000).

At weaning, *Ttpa*$^{+/+}$ mice were fed a normal diet (35 mg of dl-α-tocopheryl acetate/kg, vitE+; WT) while *Ttpa*$^{-/-}$ mice were fed either an α-TOH-deficient diet (<10 mg of dl-α-tocopheryl acetate/kg, vitE-; DEF), or α-TOH-supplemented diet (600 mg of dl-α-tocopheryl acetate/kg, vitE+++; SUPP) diet. Custom Teklad non-irradiated vacuum-packaged diets were ordered through Harlan Laboratories (Madison, WI) and were identical to those previously used in this mouse model (Finno et al., 2018, Ulatowski et al., 2014). To prevent oxidation, diets were maintained at -20°C and used within six months. Mouse diets were replaced once per week, and high-performance liquid chromatography with fluorescence detection used to confirm dietary α-TOH concentrations was performed as previously described (Finno et al., 2018).

Method Details

Neurobehavioral assessment

Examination of mechanical sensation was performed on mice at 6 months of age, when the onset of ataxia are first noticeable (Finno et al., 2018). Mice were housed under conditions of

constant temperature (20°C), light (6:00 am to 6:00 pm), and with access to food and water ad libitum. Testing apparatus was cleaned with 70% ethanol to remove animal odors before and after each test. Experiments were performed with 8-15 mice per group, consisting of ~50% male and 50% female. Each test was performed at one time point, 1-2 days before sacrifice. The von Frey filament assay was performed as previously described (Martinov et al., 2013). Mice were habituated to the experimental environment for at least 30 minutes. Briefly, von Frey filaments of increasing stiffness (0.008-1.4g) were applied on both hind paws planter surface with enough pressure to bend the filament, to determine the stimulus intensity threshold stiffness required to elicit a paw withdrawal response. A total of six recordings were performed per mouse (initial reflex, followed by five "up-down" stimuli). Dixon's score was calculated as previously described (Dixon, 1965).

Dorsal root ganglion neuron (DRGN) isolation

At 5-6 months of age, one male and one female mouse were sacrificed with pentobarbital (>100 mg/kg IP). After euthanasia, the spinal column was removed by making lateral incisions on both sides. The spinal cord was then severed at the C1 (cervical) and L6 (lumbar) vertebrae. The dorsal portion of the spinal column was removed, exposing the spinal cord. Shortly after, the spinal cord was removed to expose the DRG. Dorsal root ganglia were extracted using micro dissecting forceps and microscissors. Dorsal root ganglia were placed in a petri-dish containing 1.8 mL of ice-cold HBSS. The spines of the dorsal root ganglia were trimmed using microdissection scissors.

Following DRG removal, 200 µL of collagenase was added to the HBSS solution containing the DRG. The whole DRG were placed in an incubator for 2 hours at 37^{o}C, 5% CO_2. The DRG were subsequently transferred to a 15 ml conical centrifuge tube and washed twice with 10 mL of pre-warmed growth medium to remove any remaining collagenase solution. Collagenase is inhibited by cysteine, which is a component of the F-12 nutrient mix. The 570 mL stock solution of growth medium contained 500 mL F-12, 5 mL Pen/Strep, 5 mL 100X N2 supplement, 10 mL 50X B27 supplement, and 50 mL FBS. While in the 15 mL conical tube, DRG were triturated to dissociate the DRG into individual cells. Afterward, the volume was aspirated and filtered through a 40-µm FlowmiTM Cell Strainer. The cell suspension was slowly dripped onto 10 mL 15% BSA (bovine serum albumin), pre-warmed growth medium in a 15 mL conical tube and centrifuged at 200 x g for 20 minutes. The BSA stock solution contained 1.5 g of BSA dissolved in 10 mL of F-12. The supernatant was aspirated, leaving approximately 20 µL covering the cell pellet. In this protocol, nerve growth factor (NGF) was not used in the growth medium as NGF alters gene expression (Lindsay and Harmar, 1989).

Cell count/viability and RNA quality assurance

A hemocytometer was used to determine the viability of the cells stained with trypan blue. Once non-neuronal cells were removed using a 10 mL 15% BSA treatment and centrifuged at 200 x g, a portion of the cell suspension was aliquoted into a 0.5 mL microcentrifuge tube. Despite this treatment, some non-neuronal cells may survive the removal process. Depending on the volume of the cell suspension, a 1:1 mixture was made using 0.4% trypan blue solution. The mixture was pipetted into the V-shaped groove of the coverslip. The viable and non-viable cells in each of the four corner quadrants were multiplied by 104. To obtain the percentage of viable

cells, the following formula was used: % viable cells= [1.00 - (# of nonviable cell / # of total cells)] x 100. Samples were analyzed on an Agilent Bioanalyzer before and after library preparation to ensure quality RNA and cDNA was sequenced.

Single-cell RNA-sequencing

Barcoded 3' single-cell libraries were prepared from single-cell suspensions using the Chromium Single Cell 3' Library and Gel b ead kit v2 (10X Genomics, Pleasanton, California). Libraries were pooled and sequenced on an Illumina HiSeq4000 with pair-end 100 bp reads. Cellranger v.2.0.1 and bcl2fastq v.2.17.1.14 commands mkfastq and count were used to generate fastq files per sample, align to mm10, filter, and perform barcode and UMI counting. Analyses were conducted in R, version 3.4.4 (Team, 2018). Normalization, clustering, and calculation of TSNE (van der Maaten and Hinton, 2008) coordinates were conducted using Seurat, version 2.3.0 (Satija et al., 2018). Differential expression analyses between treatments, adjusting for sample and sex, were conducted on the filtered and normalized data using limma, version 3.32.10 (Ritchie et al., 2015). Pathway analyses were performed using Panther Pathway overrepresentation analysis (http://pantherdb.org/).

Single-molecule fluorescence in situ hybridization (smFISH) with RNAscope

Mice were anesthetized with an intraperitoneal injection of ketamine (100 mg/kg) and xylazine (10 mg/kg), and were transcardially perfused with diethyl-pyrocarbonate (DEPC)-treated phosphate buffer saline (PBS) and 4% paraformaldehyde (PFA) to preserve RNA. Dorsal root ganglia (DRG) were extracted using micro dissecting forceps and micro-scissors. Dorsal

root ganglia were placed in a petri-dish containing 1.8 mL of ice-cold DEPC-treated PBS. The tissues were trimmed using a surgical scalpel blade and were kept in a 4% PFA in DEPC-treated solution, overnight on a shaker at 4°C. Samples were sequentially dehydrated in 10%, 20%, and 30% sucrose solution at 4°C for 1 hr, 2 hr, and overnight, respectively. Samples were transferred into optimal cutting temperature (OCT) compound for a minimum of 1 hr at 4°C and then snap frozen, using a dry ice-ethanol mixture. Samples were cryo-sectioned to a thickness of 14 μm, placed onto Superfrost slides and stored at -80°C until processed.

Probe hybridization and immunofluorescent staining

Probe hybridization was performed according to the manufacturer's instructions (Advanced Cell Diagnostics, ACD). Sections were immersed in pre-chilled 4% PFA for 15 min at 4°C. Sections were then dehydrated at room temperature (RT) in 50%, 70% and twice in 100% ethanol for 5 min each and allowed to dry for 1-2 min. Fixation and dehydration were followed by hydrogen peroxide reaction for 10 min at RT then, protease digestion, using protease 4 for 30 min at RT. Slides were incubated with probes in 2 hours at 40°C. To amplify and detect signals, sections were treated as follows at 40°C: AMP1 for 30 min, followed by AMP2 for 30 min, AMP3 for 15 min, the appropriate HRP channel for 15 min, Opal dye for 30 min, and HRP blocker for 15 min. Each of these alternated with a washing step two times for 2 min at RT. Probes for *Kcnmb2, Kcnq3, Kcnv1* and *Cacna1e* and controls were obtained from ACD. Sequences of the target probes and label probe are proprietary. Detailed information about the probe sequences can be obtained by signing a non-disclosure agreement provided by the manufacturer.

For subsequent immunofluorescent staining, slides were treated with 10% blocking solution for 30 min at RT, incubated with primary antibody (Tyrosine Hydroxylase, LSbio, 1:500 dilution), overnight at 4°C, washed with TBS-0.005%Tween20 three times for 5 min each, incubated with secondary antibody (Alexa 647, Life Technologies, 1:500) for 2 hours at RT, and again washed with TBS-0-005% Tween20 three times for 5 min each. Incubation in DAPI solution for 30s at RT was performed to label cell nuclei. Slides were then mounted in Fluoromount-G and sealed under a coverslip.

Immunofluorescence

Following microdissection, the tissue was fixed at 4°C in 4% PFA in PBS and 10% and 30% sucrose at 4°C overnight, then embedded in OCT for cryo-sectioning in the cryo-mold. Sections of 10-µm were washed in PBS, permeabilized in 0.1% Triton X-100 for 10 min, and then incubated for 60 min in a blocking solution containing 10% goat serum. The sections were incubated with primary antibody overnight at 4°C in a humid-chamber. The rinsed sections were then incubated (2 hrs; RT) in a fluorescent dye-conjugated secondary antibody. The following primary antibodies were used: rabbit anti KCNQ3 (Abcam, #ab16228), rabbit anti KCNV1 (Abcam, #ab175548), mouse anti KCNMB2 (Abcam, #ab94598), rabbit anti $Ca_v2.3$ (Alomone Labs, #ACC-006), mouse anti tyrosine hydroxylase (TH; LSBio, #LS-C338121), rabbit anti TH (LSBio, #LS-C354112), rabbit anti cleaved caspase-3, -8 and -9 (Cell Signaling Technology, #9664, #8592, and #9509), rabbit anti total caspase-3 and -9 (Abcam, #ab13847, and #ab202068). Secondary antibodies were Alexa 488-conjugated affinity-purified goat anti-rabbit IgG, Alexa 488-conjugated affinity-purified goat anti-mouse IgG, Cy3-conjugated affinity-

purified goat anti-rabbit IgG, Alexa 555-conjugated affinity-purified goat anti-mouse IgG (Invitrogen and Jackson Labs). Images were captured with a Nikon A1 confocal microscope.

Isolation of DRGNs for electrophysiological recordings

Dorsal root ganglion neurons (DRGNs) were isolated from male and female mice from each experimental group. Dissected tissue was removed and placed in a solution containing Minimum Essential Medium with Hank's salt (Invitrogen), 0.2 g/L kynurenic acid, 10 mM $MgCl_2$, 2% fetal bovine serum (FBS; v/v), and 6 g/L glucose. Tissues were digested in an enzyme mixture containing collagenase type I (1 mg/mL) and DNase (1 mg/mL) at 37 °C for 20 min. After a series of gentle trituration and centrifugation in 0.45 M sucrose, the cell pellets were reconstituted in 900 mL culture media (Neurobasal-A, supplemented with 2% B27 (v/v), 0.5 mM L-glutamine, 100 U/mL penicillin; Invitrogen) and filtered through a 50-μm cell strainer for cell culture. DRGNs were cultured for 24 to 48 hrs. All electrophysiological experiments were performed at RT (21-22°C). Reagents were obtained from Sigma-Aldrich (St. Louis, MO) unless otherwise noted. A stock solution of rSNX-482 was made and (10 mM) stored at -20^{o}C.

To identify mechanosensitive DRGNs, small-diameter neurons were identified, and mechanical stimulation was achieved using a fire-polished and sylgard-coated glass pipette (tip diameter ~1-2 μm), positioned at an angle of ~60° to the DRGN being recorded. Downward movement of the probe toward the cell was driven by a piezo-electric crystal micro stage (E660 LVPZT Controller/Amplifier; Physik Instruments). The probe was typically positioned close to the cell body without any visible membrane deformation. We assessed for mechanical sensitivity using a series of mechanical steps in ~0.42 μm increments applied every 10 to 20 s, which allowed

for the full recovery of mechanosensitive currents between steps. Inward mechanically-activated (MA) currents were recorded at a holding potential of -70 mV. For voltage-clamp recordings of MA currents, patch pipettes had resistance of 2-3 MΩ when filled with an internal solution consisting of (in mM): 70 CsCl, 55 NMDGCl, 10 HEPES, 10 EGTA, 1 $CaCl_2$, 1 $MgCl_2$, 5 MgATP, and 0.5 Na_2GTP (pH adjusted to 7.3 with CsOH). The extracellular solution consisted of (in mM): 130 NaCl, 3 KCl, 1 $MgCl_2$, 10 HEPES, 2.5 $CaCl_2$, 10 glucose and 2 CsCl (pH was adjusted to 7.3 using NaOH).

Data analyses were performed using pClamp8 (Axon Instruments) and Origin software (Microcal Software, Northampton, MA) offline. The peak mechanically-activated (MA) current (I_{MA}) for each step displacement $I(X)$ was expressed in the form of the probability of channel opening (P_o of I/I_{max}) with a Boltzmann equation $P_o = 1/[1 + e^{z(X - X_{1/2})/(kT)}]$ to obtain single-channel gating force, z, and the displacement at 50% open probability ($X_{1/2}$), and T is temperature.

Current-clamp experiments

Whole-cell membrane potential recordings were performed using an Axopatch 200B amplifier (Molecular Devices, San Jose, CA). Membrane potentials were amplified, bandpass filtered (2-10 kHz), and digitized at 5-50 kHz using an analog-to-digital converter (Digidata 1200, Molecular Devices) as described earlier (Levic et al., 2007, Rodriguez-Contreras et al., 2008). Electrodes (2-3 MΩ) were pulled from borosilicate glass pipettes, and the tips were fire-polished. Extracellular/bath solution consisted of (in mM) 145 NaCl, 6 KCl, 1 $MgCl_2$, 2 $CaCl_2$, 10 D-glucose, and 10 4-(2-hydroxyethyl)-1-piperazineethanesulfonic acid (HEPES), pH 7.3. The

normal pipette/internal solution contained (in mM) 146 KCl, 1 $MgCl_2$, 0.1 $CaCl_2$, 5 ethylene glycol-bis(β-aminoethyl ether)-N,N,N′,N′-tetraacetic acid (EGTA) 4 MgATP, 0.4 NaGTP and 10 HEPES, pH 7.3. The seal resistance was typically 5-10 GΩ. Data analyses were performed using the pClamp and Origin software (MicroCal Inc., Northampton, MA). Where appropriate, pooled data are presented as means $\pm$ S.E.

Voltage-clamp experiments

Whole-cell voltage-clamp recordings were conducted at room temperature (RT) using an Axopatch 200B amplifier and filtered at 2kHz through a low-pass Bessel filter. Data were digitized at 0.5-1.0 kHz using a Digi-Data analog-to-digital converter. To study Ca^{2+} currents in DRGNs, after ~2 days in culture, the cells were held in a bath solution (in mM; 60 NMGCl, 50 CholineCl, 10 NaCl, 20 tetraethylammonium chloride (TEACl), 5 4-Aminopyridine (4-AP), CsCl, 5 $CaCl_2$, 0.5 $MgCl_2$, 10 HEPES and 5 Glucose at pH 7.4). Freshly reconstituted tetrodotoxin (TTX) (final concentration, 2 μM) was added to the bath solution to further suppression Na^+ currents. The internal solution contained (in mM) 60 Cs-gluconate, 60 mM N-methyl-d-glucamine (NMDG)-Cl, 2 $MgCl_2$, 0.1 $CaCl_2$, 5 K_2ATP, 0.5 GTP-sodium, 5 EGTA, and 10 HEPES, pH 7.35, with CsOH.

K^+ currents were measured using bath solution containing (in mM: 60 NMGCl, 35 CholineCl, 5 KCl, 10 NaCl, 0.05 $CaCl_2$, 0.5 $MgCl_2$, 10 HEPES and 5 glucose at pH 7.4). Freshly reconstituted tetrodotoxin (TTX) (final concentration, 2 μM) was added to the bath solution to suppression Na^+ currents. The pipette solution contained (in mM; 140 KCl, 1 $MgCl_2$, 10 HEPES, 2.5 EGTA, 1 $CaCl_2$, and 4 MgATP, at pH 7.2). Freshly reconstituted tetrodotoxin (TTX) (final concentration, 2 μM) was added to the external solution to suppression Na^+ current when

measuring K^+ and Ca^{2+} currents. Ca^{2+} currents were also suppressed, but not eliminated using 50 μM external Ca^{2+}

Borosilicate glass pipettes were pulled using a Sutter P-97 Flaming Brown Micropipette Puller (Sutter Instruments) and fire-polished for an optimal pipette resistance (2-3 MΩ). Access resistance was compensated further by at least 80%. After achieving a GΩ-seal, gentle suction was applied to form a whole-cell configuration. In all cases, liquid junction potentials were measured and corrected as described previously (Rodriguez-Contreras and Yamoah, 2001). Currents were activated with depolarizing voltage steps from -120 to 40 mV, using a ΔV of 10 mV and holding potentials at -40, -60 and -90 mV. All protocols were employed without online leak subtraction.

Quantification and Statistical Analysis

Statistical analysis

All data was evaluated for normality using a Shapiro-Wilk test. Parametric data were analyzed via a one-way ANOVA compared the three genotype / diet groups followed by a Tukey post-hoc test. Non-parametric data were analyzed with a Kruskal-Wallis test followed by Dunn's multiple comparison tests. For quantification of mRNA via RNA-scope, four high-power fields were evaluated from n=2-3 mice in each group and number of mRNA TH+ DRGNs quantified. For electrophysiologic recordings, n=2-3 pooled mice with 9-15 DRGNs per experimental group were recorded. Significance was set at $p < 0.05$.

Data and Software Availability

The raw and processed data for scRNA-seq individual libraries have been deposited in the NCBI Gene Expression Omnibus (GEO) under ID codes (GEO:GSE128276, GSM3670444, GSM3670445, GSM3670446, GSM3670447, GSM3670448, GSM3670449).

Supplemental References

DIXON, W. J. 1965. The Up-and-Down Method for Small Samples. *J Am Statist Assoc* 60**,** 967-978.

FINNO, C. J., BORDBARI, M. H., GIANINO, G., MING-WHITFIELD, B., BURNS, E., MERKEL, J., BRITTON, M., DURBIN-JOHNSON, B., SLOMA, E. A., MCMACKIN, M., CORTOPASSI, G., RIVAS, V., BARRO, M., TRAN, C. K., GENNITY, I., HABIB, H., XU, L., PUSCHNER, B. & MILLER, A. D. 2018. An innate immune response and altered nuclear receptor activation defines the spinal cord transcriptome during alpha-tocopherol deficiency in Ttpa-null mice. *Free Radic Biol Med,* 120**,** 289-302.

LEVIC, S., NIE, L., TUTEJA, D., HARVEY, M., SOKOLOWSKI, B. H. & YAMOAH, E. N. 2007. Development and regeneration of hair cells share common functional features. *Proc Natl Acad Sci U S A,* 104**,** 19108-13.

LINDSAY, R. M. & HARMAR, A. J. 1989. Nerve growth factor regulates expression of neuropeptide genes in adult sensory neurons. *Nature,* 337**,** 362-4.

MARTINOV, T., MACK, M., SYKES, A. & CHATTERJEA, D. 2013. Measuring changes in tactile sensitivity in the hind paw of mice using an electronic von Frey apparatus. *J Vis Exp***,** e51212.

RITCHIE, M. E., PHIPSON, B., WU, D., HU, Y., LAW, C. W., SHI, W. & SMYTH, G. K. 2015. limma powers differential expression analyses for RNA-sequencing and microarray studies. *Nucleic Acids Res,* 43**,** e47.

RODRIGUEZ-CONTRERAS, A., LV, P., ZHU, J., KIM, H. J. & YAMOAH, E. N. 2008. Effects of strontium on the permeation and gating phenotype of calcium channels in hair cells. *J Neurophysiol,* 100**,** 2115-24.

SATIJA, R., BUTLER, A. & HOFFMAN, P. 2018. Seurat: Tools for Single Cell Genomics. R package version 2.3.0.

TEAM, R. C. 2018. R: A language and environment for statistical computing. R Foundation for Stati stical Computing. Vienna, Austria.

TERASAWA, Y., LADHA, Z., LEONARD, S. W., MORROW, J. D., NEWLAND, D., SANAN, D., PACKER, L., TRABER, M. G. & FARESE, R. V., JR. 2000. Increased atherosclerosis in hyperlipidemic mice deficient in alpha -tocopherol transfer protein and vitamin E. *Proc Natl Acad Sci U S A,* 97**,** 13830-4.

ULATOWSKI, L., PARKER, R., WARRIER, G., SULTANA, R., BUTTERFIELD, D. A. & MANOR, D. 2014. Vitamin E is essential for Purkinje neuron integrity. *Neuroscience,* 260**,** 120-9.

VAN DER MAATEN, L. J. P. & HINTON, G. E. 2008. Visualizing High-Dimensional Data Using t-SNE. *J of Machine Learning Res,* 9**,** 2579-2605.